

Sensitivity analysis of rock mass discrete fracture network to UAV 3D point cloud resolution and processing parameters


JAMES MULALA

July, 2020

SUPERVISORS:

Dr. Olga. C. Mavrouli

Dr. Panagiotis Nyktas



Sensitivity analysis of rock mass discrete fracture network to UAV 3D point cloud resolution and processing parameters

JAMES MULALA

Enschede, The Netherlands, July, 2020

Thesis submitted to the Faculty of Geo-Information Science and Earth Observation of the University of Twente in partial fulfilment of the requirements for the degree of Master of Science in Geo-information science and Earth Observation.

Specialization: Natural Hazards and Disaster Risk Reduction

SUPERVISORS:

Dr. Olga. C. Mavrouli

Dr. Panagiotis Nyktas

THESIS ASSESSMENT BOARD:

Prof. Dr. Victor Jetten (Chair)

Dr. Harry Seijmonsbergen (External Examiner, University of Amsterdam)

DISCLAIMER

This document describes work undertaken as part of a programme of study at the Faculty of Geo-Information Science and Earth Observation of the University of Twente. All views and opinions expressed therein remain the sole responsibility of the author, and do not necessarily represent those of the Faculty.

ABSTRACT

Rockfalls cause a lot of destruction to life and property globally especially in hilly terrains. Photogrammetry plays an important role in monitoring of rockfalls. Both LIDAR and UAVs have been used to monitor the source areas of rockfalls and their trajectories since decades ago. The reduction in the price of drones on the market has broadened the use of the aircrafts beyond the military use. The development of discontinuity set extraction algorithms has also enabled automatic extraction and analyses of the discontinuities in a rock mass using photogrammetry data in slope stability studies. However, the existing approaches use empirical parameter values to collect photogrammetry data and extract the discontinuities from the rock mass whose results are therefore, not transferable. Hence this research aimed to develop a generic methodology of determining the optimal parameter requirements for a UAV flight plan and discontinuity sets extraction from the collected drone data. The study area comprised two slopes located within the Samaria Gorge site in Crete, Greece. Slope 1 is an upper slope east of the entrance to the gorge and slope 2 is road cut of one of the sections of the access road to the Kallergi refugee camp. The automated UAV survey was used collect data from slope 1 while at slope 2, the manual flight was employed. The UAV data was processed using pix4D to generate point clouds. The point clouds were subjected to automatic discontinuity set extraction using DSE. Three main discontinuity sets were successfully extracted by DSE. One of the three structures is horizontal and orienting in the same direction as the slope and the other two are sub vertical in both slopes. The recovered discontinuities were overlapped with the visually identified structures on the RGB point cloud to quantitatively determine the accuracy and effectiveness of the algorithm to extract the discontinuity sets in a point cloud via the computation of classification accuracy indices. The highest overall accuracy results obtained for the slope 1 data were: 40% for knn, 40% for α and 47% for β from the 2cm_GSD_45° point cloud and 33% knn, 37% α and 40% in the β parameter experiments from the 2.5cm_GSD_45° model. Conversely, the highest overall accuracies for the slope 2 data were: 73% for knn, 80% for α and 73% for the β parameter. The accuracy indices results showed that the slope 2 data outperformed the slope 1 data. The poor results in the slope 1 data were mainly due to noise in the data, insufficient exposure of the rock mass surface, too many undulations on the slope surface, occlusions and shadowing effect from the higher vegetation. The optimized parameters based on slope 2 accuracies were: knn 40, α 15 and β 50. The geometric characteristics of the discontinuities in the two slopes were predominantly tiny spacing in the order of 10cm and non-persistent in the order of 0m persistence forming a highly fragmented discontinuity network. In addition to the fragmented geological structures, rockfall triggering factors that are active and frequent in the area accelerate rockfalls down the slopes. Therefore, rockfall mitigations guided by comprehensive hazard mapping are highly recommended. Future, studies are recommended to quantitatively determine the effect of roughness on the extraction of the discontinuities, study the vegetation removal capabilities of the canupo plugin in cloudcompare to maximize its potential in such research work and lastly, future studies can consider checking the influence of other parameters not tested in this research in other terrains with different characteristics and check how the requirements of flight planning and discontinuity set extraction would change or compare with the results obtained in this research.

Key words: Rockfall, Photogrammetry, UAV, Point cloud, Discontinuities, DSE, Sensitivity, Accuracy indices, Slope stability.

ACKNOWLEDGEMENTS

My sincere gratitude go to my supervisors Dr. Olga C. Mavrouli for her critical analysis of my work and demanding nothing but quality work and Dr. Panagiotis Nyktas for his tireless help in the field during data collection without which fieldwork would have been difficult. Dr. Mavrouli, no words can ever express my gratitude for your guidance and encouragement. Dr. Nyktas, your passion and practical experience in UAV photogrammetry was inspirational. I also acknowledge the president (Petros Lymberakis) and the personnel of the management Body of Samaria – West and the Forest Directorate of Chania for the logistic support and permissions to work in the area. To Nikiforos Nikiforakis and Manolis Kontoudakis, I say thank you for lending us the GNSS pole during fieldwork. Equally, I would like to thank HxGN SmartNet and Metrica S.A for availing me the RINEX GNSS correction data. I would also like to passionately thank my wife Lucy and my daughter Lumbo for their patience, perseverance and encouragement towards my studies. I extend my thank you to my friends and classmates for their moral support. My appreciations also go to nuffic and my employer for awarding me a scholarship and leave respectively to study at the University of Twente, The Netherlands. Lastly, I thank the Almighty God for His mercies throughout my life.

TABLE OF CONTENTS

1.	Introduction.....	1
1.1.	Background.....	1
1.2.	Study Area.....	2
1.3.	Problem statement	4
1.4.	Objectives	5
1.5.	Thesis structure.....	6
2.	Literature review	7
2.1.	UAV survey	7
2.2.	Structure from Motion	8
2.3.	Discontinuity set identification and extraction	8
2.4.	Sensitivity analysis of discontinuity set extractor parameters	9
2.5.	Geometrical characteristics of discontinuities	10
2.6.	Discrete fracture network and slope stability	11
3.	UAV survey and 3D terrain model reconstruction.....	12
3.1.	Methodology	12
3.2.	Analysis and Results.....	17
4.	Rock mass discontinuity characterization: sensitivity to processing parameters and 3D model spatial resolution.....	21
4.1.	Parametric processing.....	21
4.2.	Spatial resolution sensitivity.....	36
5.	Discussion and Conclusions	38

LIST OF FIGURES

Figure 1: Location of the study area. Source: Esri.....	3
Figure 2: Rockfall mitigation measures along the access path into the gorge.....	3
Figure 3: Schematic representation of geometrical properties of the discontinuities in a rock mass. Source: Azarafza et al., 2018 adapted after (Hudson 1992).....	10
Figure 4: Methodology workflow.....	12
Figure 5: Computation of the UAV distance to the slope.....	13
Figure 6: Distribution of GCPs points during capture (left) and during image processing (right).....	14
Figure 7: Alignment of raw point clouds.....	15
Figure 8: Classifier training.....	16
Figure 9: Sections of the point clouds showing artefacts.....	18
Figure 10: Shows the displacement of the image block.....	18
Figure 11: Quality report extract showing the differences in the XYZ dimensions between the 3D model with GCPs (above) and without GCPs (below) for the 2cm_GSD_45° model.....	19
Figure 12: Surface areas covered by residual vegetation in a cloud (right) and plot of the area of the retained vegetation against the area of the cloud (left).....	20
Figure 13: Methodology workflow.....	21
Figure 14: Scanline measurements.....	22
Figure 15: Visual recognition of joints in a raw image obtained from an automatic flight on slope 1.....	24
Figure 16: Visual recognition of the discontinuities in a raw image obtained from a manual flight on slope 2.....	24
Figure 17: Selected joint sets within the selected grid on the RGB cloud of the 2cm_GSD_data from slope 1.....	26
Figure 18: Sampled joints within the selected grid on the RGB cloud of the 2.5cm_GSD_45 data from slope 1.....	26
Figure 19: Location of the sampled discontinuity sets within the selected grid on the RGB cloud of slope 2 data.....	27
Figure 20: Poor results due to noise.....	28
Figure 21: Improved results after increasing n_p	28
Figure 22: Extract of the results of overlap between the joints in the classified and the RGB clouds.....	31
Figure 23: Results of discontinuity set overlap at different knn values.....	31
Figure 24: Overall accuracies for the knn parameter on slope 1 & 2 data.....	33
Figure 25: Overall accuracies for the α parameter on slope 1 & 2 data.....	34
Figure 26: Overall accuracies for the β parameter on slope 1 & 2 data.....	34
Figure 27: Stereographic projection showing the dip/dip directions of the joint sets automatically identified.....	35
Figure 28: Stereographic projection showing the dip/dip directions of the joints manually recognized.....	35
Figure 29: Methodology workflow.....	36
Figure 30: Results of joints overlap in the subsampled classified and RGB clouds at optimal parameter values.....	36
Figure 31: Results of joints overlap in the subsampled classified and RGB clouds at knn 50 and constant α , β and n_p	37
Figure 32: Overlap results between the resampled classified and RGB clouds at n_p 500 and other optimal parameters kept constant.....	37

LIST OF TABLES

Table 1: Flight plans and the number of images captured per flight.....	13
Table 2: Number of images and point densities of the point clouds obtained against the flight plan parameters	17
Table 3: Densities of the point clouds after vegetation removal.....	17
Table 4: Results of vegetation removal by different methods.....	19
Table 5: Total areas covered by residual vegetation in each cloud after automatic vegetation removal	20
Table 6: Selected DSE parameters for parametric processing.....	22
Table 7: Explains the parameters used in the parametric processing and how they influence the results.....	23
Table 8: Confusion matrix for the discontinuity overlap classification accuracy indices at knn_{10}	29
Table 9: Confusion matrix for the discontinuity overlap classification accuracy indices at α_{15}	29
Table 10: Confusion matrix for the discontinuity overlap classification accuracy indices at β_{50}	29
Table 11: Confusion matrix for the discontinuity overlap classification accuracy indices at knn_{30}	30
Table 12: Confusion matrix for the discontinuity overlap classification accuracy indices at α_{15}	30
Table 13: Confusion matrix for the discontinuity overlap classification accuracy indices at β_{40}	30
Table 14: Confusion matrix for the discontinuity overlap classification accuracy indices at knn_{40}	32
Table 15: Confusion matrix for the discontinuity overlap classification accuracy indices at α_{15}	32
Table 16: Confusion matrix for the discontinuity overlap classification accuracy indices at β_{50}	32
Table 17: Examples of Dip/ dip direction of the joints extracted when knn values were varied while keeping others constant on the 2cm_GSD model with GCPs.....	35
Table 18: Examples of Dip/ dip direction of the joint sets recovered when knn was varied while keeping other parameters fixed on the 2.5cm_GSD model with GCPs.....	35
Table 29: Densities of subsampled clouds.....	36

1. INTRODUCTION

1.1. Background

Rockfalls cause a lot of damage to life and property globally (UNDRR, 2019). In the absence of adequate mitigation measures, rockfalls can severely ravage communities especially in hilly terrains (Gomez & Purdie, 2016; Guzzetti et al., 2002; Jaboyedoff et al., 2005; Pellicani et al., 2016; Pradhan & Sameen, 2017). Rockfall is a type of mass movement that involves free fall, sliding, rolling or toppling of a detached rock block from the parent rock mass down its slope by gravity (Fanos & Pradhan, 2018a). Rock block detachment is caused by weathering, jointing, pore pressure, erosion, earthquakes and freeze-thaw cycle (Crosta & Agliardi, 2003; Gnyawali et al., 2016). Detachment of rock blocks occurs along the discontinuities in a rock mass (Admassu & Shakoor, 2012; Wyllie & Mah, 2005). A rock mass comprises the intact rock and the discontinuities. Wyllie and Mah (2005), define discontinuities as the naturally occurring breaks in a rock and form planes of weakness in a rock mass.

Discontinuities facilitate passage of fluids in a rock mass which contribute to the reduction in shear strength of the rock mass. Therefore, geomechanical characterization of the rock mass is imperative so as to understand its properties that in turn influence the rock slope stability (Romana et al., 2003; Wyllie & Mah, 2005). Established rock slope classifications exist that help in geomechanical characterization of the rock mass. These classifications include rock mass rating (RMR) by (Bieniawski, 1973, 1984, 1989 as cited by Romana et al., 2003 pg. 1); rock quality designation (RQD) by (Deere 1967 cited by Hoek, 2006 pg. 3); slope mass rating by (Romana et al., 2003) and Slope stability probability classification (SSPC) by (Hack, 1998). Despite some drawbacks, rock mass classifications can provide reliable information such as discontinuity density necessary for planning appropriate mitigation measures against rock failure based on their thresholds. For example, slopes with SMR values of between 75 and 100 can be regarded as stable and may therefore, not need support whereas slopes with SMR values of < 30 may signal serious instability and therefore, require mitigation measures to curtail the potential slope failure (Romana et al., 2003).

Consequently, implementation of appropriate mitigations guided by geomechanical characterization can help to prevent or reduce destruction caused due to rockfalls. However, the mitigation measures can only be effective if the causes and sources of rockfalls are fully understood. Therefore, the study proposed to examine the geometrical characteristics of the discontinuities in the rock mass of the research area to properly inform the implementation of such measures and recommend a plausible semi-automated approach of carrying out such a study that generates optimal results. Lei et al. (2017), define discrete fracture network (DFN) as a model that represents the geometry of the fractures (discontinuities) in a rock mass.

In earlier decades, advances in LIDAR and photogrammetry technology have enabled robust data capture and generation of high resolution of 3D models depicting terrains of target including slopes. Improvements in the photogrammetric data capture methods, have been accompanied by development of discontinuity set identification and extraction algorithms that are replacing the manual measurements of geomechanical properties of discontinuities. The use of unmanned aerial vehicle (UAV) photogrammetry is rapidly growing in undertaking similar works though not to the same scale as the airborne LIDAR (Bühler et al., 2016; Tannant, 2015). However, the existing approaches employ empirical parameterization during both data capture and discontinuity extraction. Therefore, this study attempted to carry out a sensitivity analysis aimed at assessing the principal UAV flight plan and the discontinuity set extraction parameter requirements in order to provide an insight of the minimum parameter requirements for a standard flight plan and

discontinuity set extraction from the 3D models depicting similar terrains as the study area. Ground methods of investigating geological structures are tedious, time consuming, limit access to steep slopes and biased due to individual's preferences of what areas to examine over the others (Haneberg, 2008). Hence, the use of UAV photogrammetry to collect the survey data.

1.2. Study Area

The study area is located in the western mountain massif of the island of Crete in Greece. The research area comprised two slopes. Slope 1 is the upper slope located east of the entrance to the Samaria Gorge while slope 2 is a road cut of the access road to the Kallergi refugee camp within the gorge area. The point coordinates of the site are 35°18'27.52"N and 23°55'07.38"E. Samaria Gorge is located on the island of Crete, Sfakia Province in Greece. The gorge is bound by steep slopes. Rahl et al. (2004) described the geology of Crete as predominantly limestones and dolomites. The formation of the gorge dates back during the quaternary period (west-crete.com, 1999). The Lefka Ori (White Mountains) whose rock formations are mainly calcium carbonates such as platy marble, dolomites and limestones are the largest mountains in Crete. Most of these rocks were formed millions of years ago due to dissolution of the calcium carbonate eroded on land by surface runoffs and deposited in the riverine area. Due to unending deposition, compression and folding of the rocks impacted by the tectonic movements, as a result of the subduction zone converging the African plate and the European plate in the study area, the uplifting of the mountains continues to date reaching an altitude of 2453m above sea level at Kelf Ori and have been largely responsible for the formation of the gorges. However, the highest peak in Crete is at Psiloritis which is 3m higher (wordpress.com, n.d.). Seismic activity is prominent in the area evidenced by a 6 magnitude Richter scale earthquake that occurred during the field visit by the author on December 22, 2019.

Therefore, occurrence of rockfalls at the gorge is not unusual especially during the rainy season and routine freeze thaw cycle. Fragments of rocks and boulders were noticed especially along the access path into the gorge either trapped by the wire meshes (protective nets) or came to rest on the path as shown in figure 2. Debris flows and flash floods running down the slope surfaces were also noticed during fieldwork. Presence of faults, fracturing of rock masses, steep topography and high seismic activities lead to increased rockfall events in Greece (Saroglou, 2019). Figure 1 shows the location of the study area.

The gorge is a tourist attraction and therefore, of economic significance to the country. Region of Crete (2017) reports that between 2000 and 2008 Crete contributed about 5% to the national domestic product (GDP). The report further indicates that per capita GDP of the region equals that of the entire country whose major source of revenue is the seasonal tourism industry which contributes 30% and 25% of the total 5 and 4 star hotels in Greece.



Figure 1: Location of the study area. Source: Esri

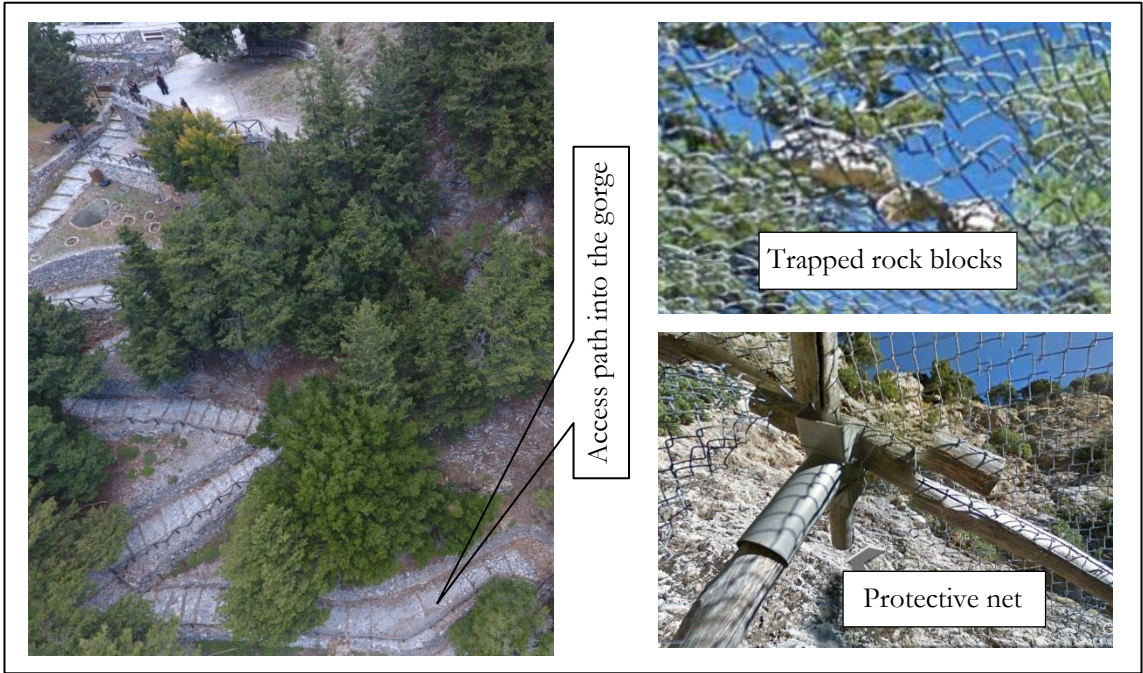


Figure 2: Rockfall mitigation measures along the access path into the gorge

1.3. Problem statement

Use of LIDAR and UAV data in geosciences has grown in popularity over the last decades. For example, Žabota et al. (2019), compared different spatial resolutions of the official digital elevation models (DEMs) for Slovenia derived from the photogrammetry data whose reference was a 1m resolution DEM in order to determine the potential source areas and run out of rock falls. The results showed that the low resolution DEMs performed better at the regional scale than the high resolution DEMs while the high resolution DEMs outperformed the coarser resolution DEMs at the local scale. These results are consistent with (Zieher et al., 2012) who also experimented the reach distance of rock falls on different resolutions of the digital terrain models (DTMs) derived from two datasets of airborne laser scanning. The results reviewed that the high resolution DTMs took into account the microtopography of the slope and produced more realistic results than the low resolution DTMs which overestimated the lateral extent of rock fall run out. Similarly, Bühler et al. (2016), observed in their simulation of the rock fall run out using unmanned aerial system (UAS) data that the finer resolution DEM stopped the blocks moving further down the slope whereas the coarser resolution DEM did not.

Further, Riquelme et al. (2014), successfully characterized the rock mass discontinuities in the 3D point cloud and performed sensitivity analysis of parameter changes without changing the resolution of the data. Nagendran et al. (2019), also extracted two major discontinuities using cloudcompare and conducted sensitivity analysis on the two discontinuity sets using the orientation data to determine the probability of failure. However, no experiments were conducted to test the effect of changing spatial resolution of the data and also the terrain characteristics from which the data was collected are unknown.

Generation of high resolution 3D models has been possible due to the technological improvements in LIDAR photogrammetry and recently UAV. A similar trend in the development of the discontinuity set identification and extraction algorithms has been observed. Traditionally, LIDAR and UAV technologies and joint set extraction software employ empirical parameterization during data capture and discontinuity set extraction. Therefore, the influence of different UAV data resolution and varying of the processing parameters on the DFN and requirements are not fully understood. Hence, this study attempted to fill this gap by developing a systematic and quantitative semi-automated approach in examining the effect of different spatial resolution of UAV photogrammetry data and processing parameter changes on the characterization of discontinuities in a rock mass in order to develop a methodology that can be applied to similar environments as the study area by providing an insight of the minimum parameter requirements for a standard flight plan and discontinuity set extraction.

1.4. Objectives

1.4.1. Main objective

To assess the effect of UAV flight plan and point cloud processing parameters on the characterization of the rock mass discontinuities.

1.4.2. Specific objective 1

Analyze the differences in the point densities of the UAV point cloud acquired according to different flight plan parameters.

Research question 1a:

Does georeferencing influence the quality of the point cloud? If yes, what is the effect on the data quality?

Research question 1b:

What is the influence of the camera location (distance) and tilt angle on point cloud density with respect to the geomechanical characterization of the rock mass?

Research question 1c:

Which vegetation removal method produces best quality point cloud depicting complex surfaces such as rocky slopes?

1.4.3. Specific objective 2

To examine the effect of different methods and parameters used on the characterization of the rock mass discontinuities in a point cloud.

Research question 2a:

What are the existing algorithms and their parameters used to generate the DFNs in a rock mass from a point cloud?

Research question 2b:

What is the effect of varying the processing parameters on the DFNs and how can the results be evaluated?

Research question 2c:

What geometric characteristics of the discontinuity sets are depicted differently at different point cloud density and their implication on slope stability?

1.5. Thesis structure

Chapter one: Introduction

Chapter one discusses the background of the research, study area, problem statement and objectives.

Chapter two: Literature review

This chapter examines the past work related to the research.

Chapter three: UAV survey and 3D model reconstruction

Chapter three discusses the methods used to collect UAV data, image processing, georeferencing and 3D model reconstruction and the results thereof.

Chapter four: Rock mass discontinuity characterization: sensitivity to processing parameters and 3d model spatial resolution

The details of the methods used to automatically identify and extract the discontinuity sets and the results thereof are discussed in this chapter. Sensitivity analysis of different parameters during processing of the point clouds of different point density to facilitate extraction of geological structures is also discussed.

Chapter five: Discussion and Conclusions

This chapter explains the research questions and the responses to the questions, methods used to answer the research questions and the results obtained. Argumentation to support the responses to the research questions is also provided. An overview of the challenges of the research is presented in this chapter. Lastly, the final chapter discusses whether the objectives of the research were achieved or not and recommends areas of future research.

2. LITERATURE REVIEW

2.1. UAV survey

Advances in aerial photogrammetry have enabled acquisition of geospatial data from complex terrains with reasonably good precision and accuracy (Fanos & Pradhan, 2018b; Gomez & Purdie, 2016; Hugenholtz et al., 2013; Lee & Sung, 2016; Menegoni et al., 2019; Nesbit & Hugenholtz, 2019; Oniga et al., 2018; Pepe et al., 2018; F. Remondino et al., 2012). Aerial photogrammetry includes the use of UAVs and airborne LIDAR. UAVs are operated without a pilot on board but monitors and controls it from the ground (Gomez & Purdie, 2016). Drones provide low cost remote sensing solutions as LIDAR is expensive and therefore, not economical for local applications (Gomez & Purdie, 2016; Menegoni et al., 2019; Nesbit & Hugenholtz, 2019; Remondino et al., 2012; Riquelme et al., 2014).

The advent of UAV technology and subsequent reduction in its price on the market, has broadened its use for the scientific purposes beyond the traditional military use. The UAVs are increasingly being used for mapping of landscapes, hazards, emergency response, transporting and delivery of materials to inaccessible areas and secluded communities (Gomez & Purdie, 2016; Hackney & Clayton, 2015). For example, Nagendran et al. (2019), employed a drone in their rock slope characterization study in order to obtain the primary data for the rock slope stability assessment. Hackney and Clayton (2015) indicated that due to the coarse spatial and temporal resolution of the conventional satellite images, quick and detailed analysis of the topography is hampered hence, the use of UAVs, provides an immediate solution to this problem as a drone can quickly be deployed and landed at any location repetitively. The drone technology provides an option of generating a flight plan for the execution of an autonomous image acquisition mission. Further, live views are possible with UAVs to check what the drone sees as it hovers over the study area (Hackney & Clayton, 2015). Data acquisition using UAV involves manual or automated flying of the drone mounted with a camera over the study area to scan the scene under investigation and capture images of the scene being studied (pix4D, 2011; SPH-Engineering, 2019). Despite the immense advantages of UAVs, there are limitations to the use of the drones. Some of the limitations include the inability of the UAV cameras to view below the leaves in a vegetated area leading to occlusions and shadowing effect in the data, limited payload resulting in the inability of the drone to carry large sophisticated cameras, legal restrictions and bad weather conditions such as wind, rain, fog and low illumination (Anders et al., 2019; pix4D, 2011; Yilmaz et al., 2018).

UAV survey commences with preparation of a flight plan to establish the waypoints, route, nominal ground sampling distance (GSD), flight height, image overlap, camera tilt angle and the extent of the area to be scanned by the aircraft. Flight planning affects data acquisition and quality and therefore, its importance cannot be overemphasized. Environmental factors such as rain, wind, cloud cover, sun, fog, physical obstructions, vegetation, characteristics of the object to be scanned and the legal requirements should also be factored into flight planning (Jaud et al., 2019; Nesbit & Hugenholtz, 2019; Pepe et al., 2018; pix4D, 2011; Remondino et al., 2012; SPH-Engineering, 2019).

The aircraft is flown over the study area following the predetermined flight plan while the pilot monitors and controls the vehicle from the ground during data capture. The global navigation satellite system (GNSS) receiver onboard the drone captures the location of the images in space and the photos, therefore, the location of the drone at the time of image acquisition is saved in the details of the images (Gomez & Purdie, 2016; Remondino et al., 2012; Salvini et al., 2017). However, owing to the poor quality of the GNSS receiver onboard the drone, the accuracy of the model is low (Manconi et al., 2019; Menegoni et al., 2019).

Incorporating ground control points (GCPs) during image processing improves the accuracy of the 3D models (ELtohamy & Hamza, 2009; Gerke & Przybilla, 2016; Oniga et al., 2018; Sanz-Ablanedo et al., 2018).

Menegoni et al. (2019) submitted that UAVs are extensively used in rockfalls monitoring and susceptibility mapping. Deployment of a drone or a swarm of UAVs over the study area enables rapid collection of the scans and 3D reconstruction of the scene for quick decision making. Rockfalls usually occur very fast and therefore, do not provide sufficient lead time for immediate response. Therefore, the most reliable ways to prevent or control rockfalls is through implementation of active or passive mitigation measures. Effective implementation of mitigations are driven by accurate identification of the causes and source areas of rockfalls. In turn, accurate detection of the causes and sources of rockfalls requires precise and accurate mapping of the affected areas. Traditionally, ground methods such as site field visits, infrared thermography and terrestrial photogrammetry are used to map rockfall hazard prone areas by visually assessing the area and conducting contact or indirect measurements using field equipment. However, ground methods have limitations which include human errors and bias, inability to reach inaccessible areas and limited scope, etc. (Slob et al., 2007).

Manconi et al. (2019) also experimented the effect of both nadir and oblique UAV image capture on the spatial resolution of the terrain models depicting steep slopes. The authors used an external DEM from Ardupilot that had better spatial accuracy than the commonly used low resolution global DEMs such as the shuttle radar topography mission (SRTM) and the terrain following option of the flight planning software to maintain a constant UAV distance to the slope in order to reduce the effect of height changes resulting in distortions and inaccurate results and also risk of ramming the drone into the slope. The results showed differences in the point density in the two experiments. In the nadir looking experiment, a 10 million points point cloud was obtained whereas in the oblique image acquisition experiment generated a 28 million points 3D model. This is consistent with the findings of (Kozmus Trajkovski et al., 2020) who conducted a similar experiment using a national 5m resolution DTM for Slovenia.

Wyllie and Mah (2005) state that rockfalls occur along the planes of weakness referred to as discontinuities in a rock. Therefore, effective control of rockfalls, requires accurate identification and characterization of the discontinuities through the use of robust methods such as aerial photogrammetry (Haneberg, 2008).

2.2. Structure from Motion

Structure from motion (SfM) is the acquisition of 2D images in motion or from different location but capturing the same scene and reconstructing a 3D model of the captured scene from the collected 2D images (Remondino et al., 2017; Tannant, 2015; Wei et al., 2013). The 3D products from SfM include point clouds, texturized mesh, digital surface model (DSM) and orthoimage (Menegoni et al., 2019). 3D model reconstruction of the real scene is achieved by creating the 3D geometry of a scene and tracking camera poses. 3D modelling improves visualization of the specimen under study including the discontinuities in a rock mass (Wei et al., 2013). Using SfM and Multiple view stereo (MVS), a sparse and dense point cloud can be generated respectively. Further, advances in the image stitching algorithms incorporated in the image processing software like pix4D, Agisoft, Inpho, Photoscan and PhotoModeler, has immensely improved the processing speed, 3D model accuracy and removal of outliers during image 3D model reconstruction (Tannant, 2015).

2.3. Discontinuity set identification and extraction

Typically, manual methods are employed to collect information about the geometrical properties of the discontinuities in the field using the scanlines and geological compass. However, the manual methods have serious drawbacks such as difficulties in accessing steep slopes, human bias, limited scope, inaccurate results

due to knowledge gaps, exposure to rockfall hazard, etc. (Slob et al., 2007; Tannant, 2015; Wyllie & Mah, 2005). The solution to these challenges therefore, lies in the development and use of automated methods of discontinuity identification and extraction.

Recognition of discontinuity sets in a 3D model is twofold, manual and semi-automatic or automatic. The flexibility of the photogrammetric 3D models in being able to be measured either automatically, semi-automatically or manually supports the two fold discontinuity set identification and extraction methods from such datasets. Manual identification of the fractures involves visually identifying the discontinuity sets with or without the help of a planar stereoscopic mirror (Menegoni et al., 2019) while the automated method involves the use of algorithms such as discontinuity set extractor (Riquelme et al., 2014) and qFacets (Dewez et al., 2016). Recognition of the joint sets in the 3D models is facilitated via segmentation of the point cloud using various data structures such kd, octree and Delaunay triangulation. The nearest neighbour and principal component analysis (PCA) are the principal methods employed during segmentation in order to determine the coplanar and non-coplanar surfaces by establishing different cohorts of the data points in the point clouds (Dewez et al., 2016; Riquelme et al., 2014; Slob et al., 2007; Vosselman & Maas, 2010). After the automatic identification and extraction of the discontinuity sets, the geological structures are visualized in software such as cloudcompare among others to provide meaningful understanding of the structures being studied (Dewez et al., 2016; Riquelme et al., 2014; Slob et al., 2007). The discrimination of the discontinuity sets in a rock mass is based on the spectral information of the scanned object derived from the RGB camera (Spreafico et al., 2017).

2.4. Sensitivity analysis of discontinuity set extractor parameters

Riquelme et al. (2014) developed a three step methodology for semi-automatic extraction of discontinuity sets from 3D LIDAR data using the discontinuity set extractor (DSE) algorithm developed by Riquelme. The three steps are: local curvature calculation which involves nearest neighbourhood points search and coplanarity test, the second stage being statistical analysis which involves principal pole estimation and normal vector calculation to generate principal orientations of the 3D points in a plane and the third being clustering to enable class identification of the planes. The authors conducted sensitivity analysis of the algorithm on two different datasets: set A comprising scanned solid objects of different shapes while set B consisted of LIDAR data of a real scene. The study concluded that better results in set A were obtained at k – nearest neighbour (knn) value of 10, tolerance of 20%, minimum angle (θ) between two principal normal vectors of 20° and maximum angle (φ) between the normal vector of the principal pole (central point) and the normal vector of the assigned poles of 30° . In the second dataset, the authors concluded that small knn values e.g. $knn < 15$ introduced a lot of noise in the computation of principal poles while larger knn values e.g. $knn > 30$ smoothed the local curvature. On tolerance, the authors established that tolerance values less than 15% significantly discarded a number of similar points to coplanar points while values more than 25% incorporated both edge points and coplanar points into the results. Therefore, in order to strike a balance between resolution and accuracy, the optimal knn value was defined between 15 and 30 while the tolerance value set to 20%. Further, since it is generally agreed that if a set of principal components have 80% or more of variance then the data is properly represented and the 20% tolerance is therefore, acceptable (Rencher & Christensen, 2012 as cited in Riquelme et al., 2014 p. 41). Like in set A, the optimal values for θ and φ were set to 20° and 30° respectively. The algorithm employs two parameters to cluster the subset points in a plane namely the maximum distance between two points to consider a point as nearest neighbour and secondly the minimum number of nearest neighbourhood points to a point to consider the point a core or seed or central point.

However, the point density of the data used by the authors and the characteristics of their study area are unknown and the parameters values for the sensitivity analysis were empirically obtained. Further, the

geometrical characteristics of the rock mass discontinuities are not described to properly guide in parameter tuning in order to obtain optimal results. For example, if the rock mass consists of platy limestone and rough, the parameters of the discontinuity set extractor algorithm will need to be optimized so as not to grow the plates into one region thereby giving inaccurate results about the density and geometry of the discontinuities. Hence, the results obtained are not global and therefore, not transferable.

2.5. Geometrical characteristics of discontinuities

Wyllie and Mah (2005) define discontinuities as naturally occurring breaks in a rock mass and categorized them as follows:

Faults – a fracture with a noticeable movement and occur as parallel or sub parallel sets along the extent of the displacement.

Bedding – this is surface that spans parallel to the surface of deposition, a common feature in sedimentary rocks.

Foliation – this is as a result of accumulation of platy or banding minerals in metamorphic rocks.

Joints – this is a fracture in which there is no observable displacement and intersect primary surfaces such as bedding planes or other joints.

Discontinuities can reduce or increase the overall strength of the rock mass and hence its stability depending on the type, persistence, spacing, infilling and orientation of the discontinuities (Admassu & Shakoor, 2012; Agliardi et al., 2013; Wyllie & Mah, 2005). Discontinuity spacing defines the size and shape of the blocks to be detached from the parent rock and gives an indication of a type of failure to occur such as planar, wedge and toppling in a rock mass. Further, spacing of discontinuities affects the strength of the rock mass, for example, fractures closely spaced join to form an uninterrupted zone of weakness in a rock mass. Persistence is another geometrical property of discontinuities that directly influences the stability of a rock mass. Combined with discontinuity spacing, persistence also determines the size of the detached rock blocks and therefore, an important factor in determining the magnitude of the rockfall hazard. Continuous persistence severely weakens the rock mas than the non-persistent discontinuities (Wyllie & Mah, 2005).

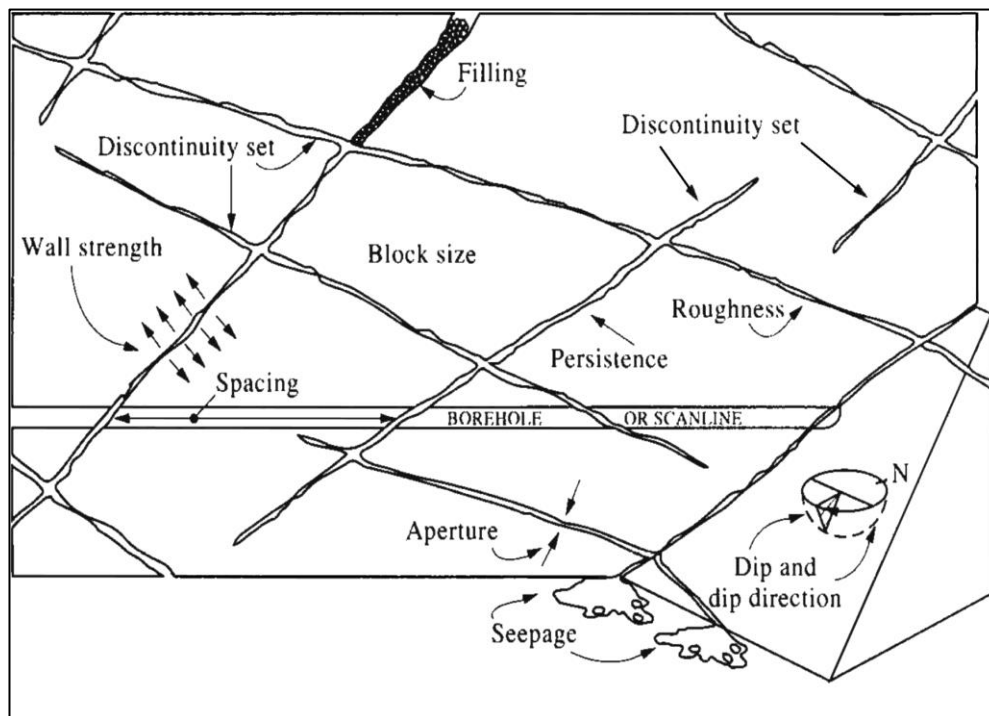


Figure 3: Schematic representation of geometrical properties of the discontinuities in a rock mass. Source: Azarafza et al., 2018 adapted after (Hudson 1992).

2.6. Discrete fracture network and slope stability

Discrete fracture network is a stochastic representation of the geometrical properties of discontinuities in a rock mass (Lei et al., 2017; Salvini et al., 2017). Salvini et al. (2017) used the DFN to interpret the fracture data collected through exposure mapping and develop a synthetic rock mass (SRM) model. The model eliminated the challenges of incorrectly interpreting to which set the discontinuities belonged and their geometrical properties due to limited or non-exposure of rock outcrops to facilitate direct observations. Further, the discontinuities are subject to in-situ stress fields in the subsurface resulting in the development of complex typologies such as cross cutting, abutting, branching, termination, bends, spacing and clustering that exacerbate the difficulties in collecting 2D/3D information using direct observations (Fadakar Alghalandis et al., 2017; Lei et al., 2017; Salvini et al., 2017).

Fadakar Alghalandis (2017) simulated the influence of discontinuity intersections, clustering network and connectivity on the stability of a rock mass and observed that these typologies play an important role on rock slope instability leading to rock slope failure as they facilitate the passage of fluids in a mass of rock.

Admassu and Shakoor (2012), Agliardi et al. (2013) and Wyllie and Mah (2005) demonstrated different rock slope failure mechanisms based on the dip/dip direction and spacing of the discontinuities. The main failure types discussed are toppling, planar and wedge.

Planar failure – planar failure occurs when the discontinuity set(s) orient parallel to the slope face and the dip angle of the fractures is less than the slope angle.

Wedge failure – occurs when two discontinuities striking parallel to the slope face intersect and dip at an angle less than the slope angle.

Toppling failure – toppling occurs when the discontinuities dip into the slope face and are within 10° of the dip direction of the face so that a series of rock blocks are formed parallel to the slope surface of a rock mass.

3. UAV SURVEY AND 3D TERRAIN MODEL RECONSTRUCTION

3.1. Methodology

Research specific objective 1 was achieved through a multi stage approach that involved field preparations, UAV flight planning, data capture, georeferencing, image processing and vegetation removal from the

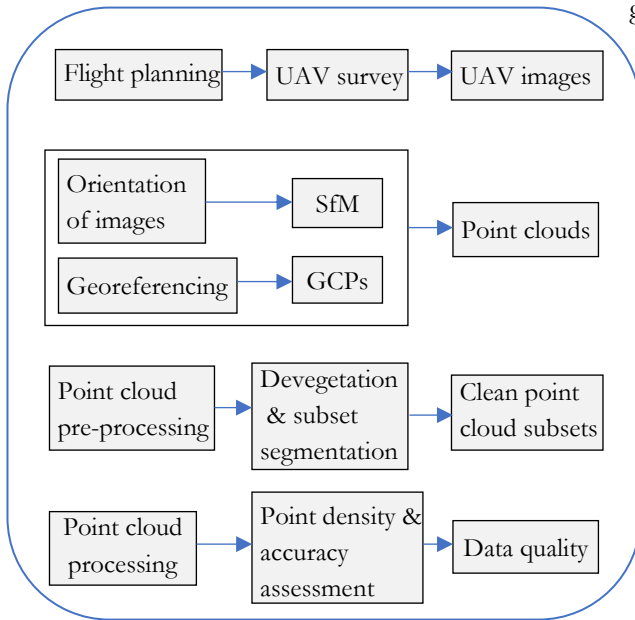


Figure 4: Methodology workflow

generated models whose outcomes were rigorously examined to obtain and prepare good quality UAV data required in the parametric processing and spatial resolution sensitivity analysis. Figure 4 summarizes the workflow of the methodology used to achieve the research sub objective 1.

tool used for a wide range of land surveying including steep slopes, area scan mainly used for surveying flat terrains and lastly, the façade scan tool suitable for preparing flight missions to survey vertical structures like buildings. Further, UgCS provides an option of generating a flight plan for the execution of an autonomous image acquisition mission, live views to check what the drone sees as it hovers over the study area (Kozmus Trajkovski et al., 2020; Manconi et al., 2019). The most important reason for the selection of UgCS in this application was that it allows for the complete customization of the flight planning keeping a constant distance from the terrain using the default SRTM DTM or an external local scale DEM to enable preparation of a more accurate flight plan. Using the photogrammetry tool, six flight plans were created with pre-set camera angles and UAV distance to the slope in order to achieve good precision and accuracy during image capture (Nesbit & Hugenholtz, 2019). Flight planning was also guided by the obstacle avoidance and legal requirements.

3.1.2. UAV Flight distance to slope and oblique view angle

In studying the use of the drone to survey a coastal cliff face and selecting the best view camera angle, Jaud et al. (2019) concluded that in order to avoid occlusions as a result of the obstruction from the cliff off nadir imaging angles of 20°, 30° and 40° were used and produced satisfactory results. Nesbit and Hugenholtz (2019) also stated and acknowledged that the use of oblique images in digital photogrammetry significantly improves the spatial accuracy, precision and reduces the amount of missing data and systematic errors in the data. In this research, the drone perpendicular distance to the slope during data capture was manually computed using the flight heights of the drone automatically generated by UgCS and the slope angle obtained from the field measurements as depicted in figure 5.

However, the drone perpendicular distance to the slope computations using the slope angle from field measurements however, were replaced by the computations using the more accurate average slope angle

manually obtained from the generated point cloud in order to minimize the large margins of error associated with the inaccuracies of field measurements regarding the exact position of the drone in space during image capture (Slob, 2010). The computed distances were 38.7m corresponding 30° camera tilt angle, 36.3m corresponding to 45°, 36.6m corresponding to 60° under the flight height of 46.5m Under the flight height of 58m the calculated UAV perpendicular distances to the slope were: 45.3m corresponding to the 30°, 45.6m corresponding the 45° and lastly 48.3m corresponding to the 60° camera tilt angle as indicated in table 1 below.

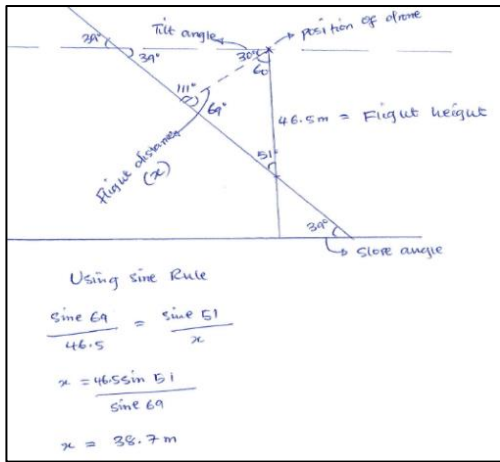


Figure 5: Computation of the UAV distance to the slope

Table 1: Flight plans and the number of images captured per flight

Flight height (m)	UAV distance to slope corresponding to oblique angle (m)			Flight mission using local scale DEM	Oblique camera angle off nadir		
					30°	45°	60°
46.5	30°	45°	60°		88	97	97
	38.7	36.3	36.6				
58	30°	45°	60°		111	111	112
	48.3	45.6	45.6				

3.1.3. Data capture

After the preparation of the flight plans, the automated surveys were executed by flying the quadcopter drone mounted with an RGB camera over slope 1 while monitoring and controlling the vehicle from the ground to scan the area under investigation in accordance with the specifications of each of the individual six flight plans. The photos were captured using trigger by distance camera control action defined during flight planning. The use of the external DEM enabled the drone to maintain a perpendicular distance to the slope and avoid crushing the aircraft into the slope by following the terrain of the slope. Other control actions included stop and turn, overshoot, take-off and landing. Stop and turn enabled the drone maintain its flight path by slowing down its flight speed and turn when joining another route. This was necessary to ensure consistent image overlap. Overshoot on the other hand is simply adding extra segments to the ends of the survey lines to allow the UAV sufficient time to turn to another waypoint especially when the stop and turn control action and action to trigger were used otherwise the drone could easily ignore some waypoints resulting in blurred images. Lastly, the take-off and landing control action allowed deployment

and landing of the UAV with or without intervention of the operator. After the execution of the automated survey, the manual flight was also conducted on slope 2 to scan the area.

3.1.4. Image processing

The images acquired during the UAV survey were processed using the pix4D software using standard and high resolution parameters to generate two sets of point clouds and subsequently select the data with the optimal quality for further processing and analysis. The first set was produced using high point density and 3D textured mesh parameter set to high resolution with $\frac{1}{2}$ image scale. The second batch was processed using the standard parameters i.e. optimal point density, $\frac{1}{2}$ image scale and the 3D textured mesh set to medium resolution. $\frac{1}{2}$ image scale uses half the size of the image to compute the additional 3D points (pix4D, 2011).

3.1.5. Georeferencing

Fourteen GCPs were captured in the kinematic mode and stored as rinex files in the GNSS receiver antenna which were later extracted using the rinex files from the tuc base station in Greece managed by METRICA S.A. Correction and extraction of the GCPs was executed using the RTKlib version 2.4.2 an open source program package for GNSS via RTKpost for post processing of the GCPs. Navigating to the options menu in the RTKpost main dialog box and pushing the setting 1 menu in the options dialog box, the frequencies/filter type was set to combined keeping the other parameters unchanged and the base station was set to Rinex Header Position using the positions menu (Bad Elf, 2020; RTKLIB, 2011). Since the GNSS receiver was set in the kinematic mode, the device obtained coordinate readings every second, hence, to obtain the fourteen individual readings, the readings were averaged based on the time lapse between the consecutive points. Figure 6 shows the distribution of the fourteen GCPs on the peripherals of the study area. It is worthwhile to note that the GCP locations were only taken around the take-off and landing area of the aircraft (base of the slope) and along the northern boundary of the study area due to too steep terrain and forest cover of the study area that impeded accessibility to other areas of the slope.



Figure 6: Distribution of GCPs points during capture (left-red dots) and during image processing (right-blue marks)

The images were directly georeferenced using the GNSS coordinates on board the UAV platform (Salvini et al., 2017). However, the accuracy of the UAV GNSS sensor may be impeded by poor satellite reception due to for example, bad weather, cloudy condition, structural obstructions such as buildings, trees and hilly terrain (Manconi et al., 2019; Menegoni et al., 2019). Therefore, the fourteen GCPs were incorporated during the processing of the images to improve the accuracy of the 3D models (ELtohamy & Hamza, 2009; Gerke & Przybilla, 2016; Oniga et al., 2018; Sanz-Ablanedo et al., 2018). Due to improper location of some GCPs, the bad GCPs were removed retaining five good ones as shown in the right image in figure 6 because the negative effect of bad location of GCPs on the spatial accuracy of the model is worse than the number of GCPs (ELtohamy & Hamza, 2009; pix4D, 2011). Of the five, three GCPs were used as check points (CPs)

to assess the absolute accuracy of the model by independently verifying the image location error and by not taking part in the bundle block adjustment (pix4D, 2011; Sedorovich et al., 2010).

3.1.6. Vegetation removal

Unlike airborne LIDAR whose laser beam can penetrate between leaves when scanning a vegetated study area, UAV optical cameras lack such capabilities hence, leading to occlusions and shadowing effect in the data especially below the canopy and behind the obstructed areas (Anders et al., 2019; Isenburg, 2014; Vosselman & Maas, 2010; Yilmaz et al., 2018). Besides the traditional manual method, several automatic vegetation removal methods exist to enable automatic removal of vegetation from the vegetated 3D datasets. These algorithms include cloth simulation filter (CSF), a plugin in cloudcompare developed by Zhang et al. (2016), LAStools developed by Isenburg (2014) and CANUPO another plugin in cloudcompare developed by Brodu and Lague (2012). Vegetation removal was necessitated by the need to expose the terrain of slope 1 to facilitate proper parametric processing.

3.1.6.1. Area of interest segmentation

Subsets of a representative area within the study area in the generated point clouds were segmented out to facilitate vegetation removal. To obtain the segments of the same size and shape, all the point clouds were

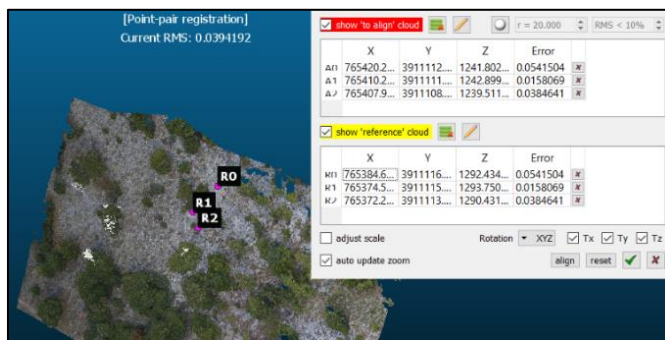


Figure 7: Alignment of raw point clouds

sequentially aligned in pairs of two as compared to reference point clouds as illustrated in figure 7, via the alignment tool in cloudcompare and the selected subsets were segmented out at once. Segmentation of the subsets was carried out in order to narrow down to a specific area of interest within the study area and also to rid the data of excess vegetation and other artefacts.

3.1.6.2. Application of vegetation removal methods

3.1.6.2.1. Manual segmentation

Manual removal of vegetation was executed via the segmentation tool in cloudcompare. The vegetation was segmented out of the point cloud either singularly or in batches convenient to the operator. Good results were achieved by tilting or rotating the point cloud close to 90° in order to clearly visualize the separation between the canopy of the vegetation and the ground. This enabled clear segmentation of the stems leaving the ground untouched depending on the height of the vegetation. Though tedious, this method achieved better results and was used as a reference to the automatic methods in this research.

3.1.6.2.2. Cloth simulation filter (CSF)

CSF is a plugin in cloudcompare developed by Zhang et al. (2016) and removes vegetation by classifying vegetation as non-ground points and the terrain as ground points based on the classification threshold. CSF is accessed via plugins tool. Since the study area is a slope, the general parameter was set to steep slope while the advanced parameters cloth resolution (grid size) and classification thresholds were set to 0.1m and 0.5m respectively to obtain the best results. The other parameter value combination tested were 2.0 for the grid size and 0.5 for the classification parameter, the third batch had 0.1 and 0.1 while in last batch the thresholds were set to 0.1 and 1.0 respectively. The maximum iterations parameter was maintained at 500 as it had little or no effect on the results.

3.1.6.2.3. LAStools

LAStools is a software suite created by Isenburg (2014). LAStools incorporates among others two important tools namely lasground and lasclassify used to separate and classify ground points and non-ground points respectively. The pipeline used in LAStools to filter out vegetation from the terrain models is firstly, apply lasground to separate ground and non-ground points, then subject the results to lasheight to compute the height of each 3D points in the cloud and lastly apply lasclassify to classify the separated points into terrain points and non-ground points (vegetation) respectively. The optimized parameters for lasground were step (grid size) = 1m and 2m and offset (threshold above ground) = 0.5m while the parameters used for lasclassify were step (grid size) = 4m and offset (threshold above ground) = 0.1m. The results were visualized in cloudcompare to check the number of points left after vegetation removal.

3.1.6.2.4. CANUPO

CANUPO (Brodu & Lague, 2012) is a plugin in cloudcompare used for supervised classification. Two sets of four training samples each for vegetation and ground points (terrain) respectively were selected via segmentation > edit > merge tool to create a classifier. The classifier was then used to classify all the other point cloud subsets. The point cloud obtained from the 48.3m perpendicular distance to the slope at a tilt angle of 60° was selected and used for the creation of a classifier because it had the most vegetation. The parameter values used were ramp minimum = 0.1 while maximum was set to 1.0 and step or grid = 0.1.

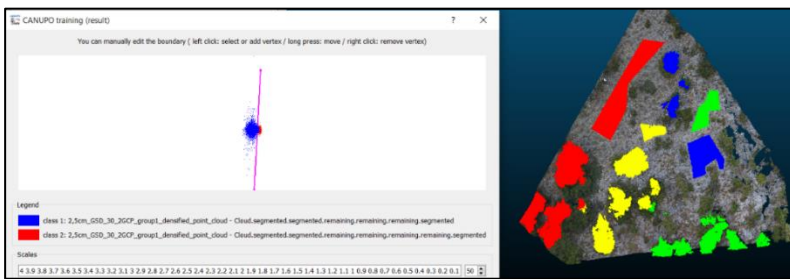


Figure 8: Classifier training

The second batch of parameters consisted of minimum = 0.1, step = 0.1 and maximum = 2.0. The last set had minimum set to 0.1, step to 0.1 and maximum to 5.0. The dimension value used was 2 and the tested scales were set to 10 and 6 respectively.

3.1.6.3. Evaluation of the vegetation removal methods

The pre-processed point cloud subsets were subjected to quality assessment procedure to assess the effectiveness and suitability of the automatic vegetation removal methods. The quality assessment process involved calculation of areas covered by residual vegetation retained after application of the vegetation removal method and results compared to the manual method (reference). The area computation was executed via the tools menu in cloudcompare and fitting a 2D polygon (facet) on the residual vegetation and automatically computed the areas covered by vegetation. The point clouds with highest point density were selected as candidate datasets for the computation of areas covered by the residual vegetation. Cloud-to-cloud distance computation was also carried out to determine the effectiveness of the methods to retain the ground points in the point clouds. Cloud-to-cloud distance computation establishes the nearest distance of points in the compared point cloud to the points in the reference point cloud. The mean distance between the points between the compared and reference point clouds should cluster around zero on the scaler field bar or histogram. If the mean distance is skewed away from zero then the margin of error in the compared point cloud is high and therefore, the data quality is low (Girardeau-Montaut, 2015). The C2C computation results are attached in appendix 2c.

3.2. Analysis and Results

3.2.1. Flight planning, data capture and UAV perpendicular distance to the slope

The six flight plans were successfully executed on slope 1 and a total of 616 UAV images were collected as tabulated in table 2. Further, 49 images were collected using a manual flight from slope 2. The slope 1 images were collected in accordance with the specifications of the individual flight plans as shown in table 1 above. The vertical and horizontal accuracies of the image coordinates were within 5m and 10m respectively. Oblique drone distances to slope were used during image capture instead of the conventional nadir looking distance because the target terrain is a slope hence it being ruled out (Jaud et al., 2019; Kozmus Trajkovski et al., 2020; Manconi et al., 2019; Nesbit & Hugenholtz, 2019).

Table 2: Number of images and number of points of the point clouds obtained against the flight plan parameters

Distance (m)	Tilt angle	Nr. images	Nr. points in model with GCPs	Nr. points in model without GCPs
36.3	45°	97	7,083,802	7,107,229
36.6	60°	97	6,968,973	6,977,138
38.7	30°	88	6,364,464	6,363,581
45.3	45°	111	7,834,736	7,827,949
45.6	60°	112	8,125,031	8,117,623
48.3	30°	111	6,667,147	6,654,033

Analysis of the results in table 2, shows that the point cloud with the highest number of points was obtained at the UAV perpendicular distance to the slope of 45.6m and camera tilt angle of 60° and the lowest having been obtained at the perpendicular distance of 38.7m with a tilt angle of 30°. However, the number of points results do not necessarily represent the actual point densities of the bare earth 3D models. The differences in the number of points of the raw point clouds is attributed to inconsistency in the distance between the overlapping images with extreme slanting view angle along the slope terrain during image capture that lead to missing data in badly overlapped images (Manconi et al., 2019). Point densities of the models obtained after removing vegetation from the clouds are tabulated in table 3.

Table 3: Densities of the point clouds after vegetation removal

Flight distance (m)	Tilt Angle	Density @ 50% of total number of points in a point cloud	
		Experiment with GCPs	Experiment without GCPs
		Density (pts/m ²)	Density (pts/m ²)
38.7	30°	631	704
36.3	45°	682	777
36.6	60°	622	694
48.3	30°	321	323
45.3	45°	382	392
45.6	60°	381	418

Review of the generated models after vegetation removal shows that flying a drone at a flight distance of 36.3m to the slope with a tilt camera angle of 45° which is coded as 2cm_GSD_45° model for easy reference under the flight height of 46.5m obtains the best point density of the point cloud as shown in table 3. The lowest point density was obtained at 48.3m with the camera oblique angle of 30° coded as 2.5cm_GSD_30° model under the flight height of 58m. Qualitative analysis of the datasets reveals more shadowing effect from the higher vegetation on the models generated from the data acquired from the lower

flight distances as compared to the data obtained from the higher distances in all the experiments. This is attributed to the increased obstruction by the target object to the view angle of the UAV camera coupled with the smaller FOV of the camera at shorter distance to the target object. However, occlusions (data gaps) were visible in all the datasets regardless of the flight distance and tilt angles.

3.2.2. Image processing

High and medium resolution point clouds were generated as shown figure 9 below. A cross check on the data showed that the presence of spurious artefacts is more pronounced in the high resolution data. Artefacts affect the accuracy of the results and therefore require removal from the data. Therefore, the high resolution point clouds were discarded and the medium resolution maintained as dataset to be used in the subsequent analyses in this research.

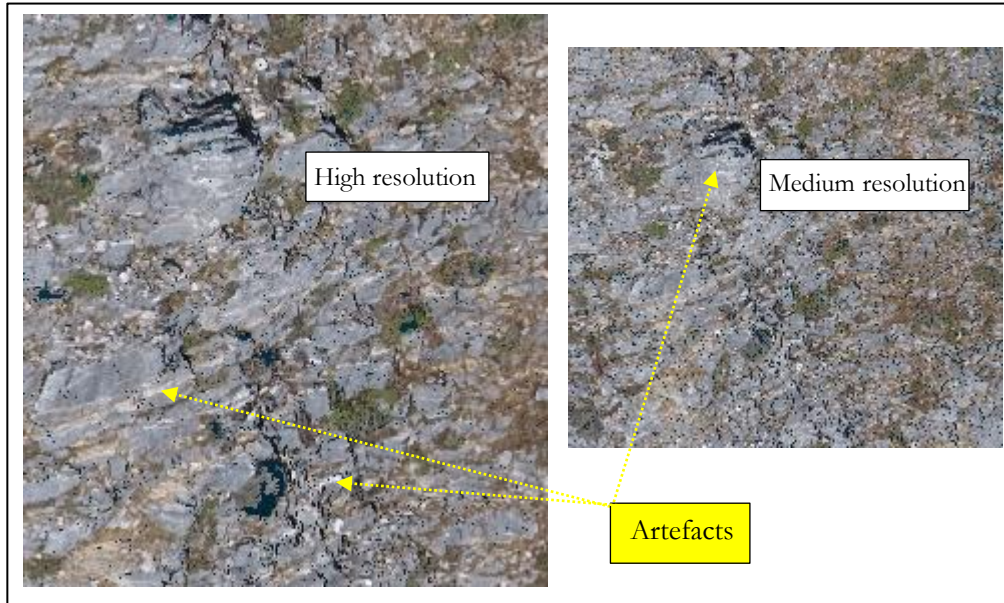


Figure 9: Sections of the point clouds showing artefacts.

The processed UAV data, comprised two datasets of point clouds corresponding to the six flight plans. One set consisted of point clouds precisely georeferenced using GCPs and another set without GCPs. The average ground sampling distances of the generated models ranged from 1.73cm to 5.73cm. Spatial accuracy expressed by the root mean square error (RMSE) of the georeferenced 3D models ranged from 0.001m to 0.03m as shown in appendix 1. RMSE is the measure of deviation from the truth. The larger the RMSE the larger the deviation and the inaccurate the results. Conversely, the smaller the RMSE the more accurate the spatial accuracy of the model. The results show that georeferencing with GCPs had an effect on the spatial accuracy

of the model by positioning the image block in the correct geographical position by pinning it to the ground to avoid stretching or warping (Nelms et al., 2018) as seen by the shift of the block from the initial position to its final position in space after applying the GCPs as shown in figure 10. This is consistent with the trend in the results of the differences in the average XYZ dimensions obtained in the image processing quality report as shown in figure 11. The differences computed from the XYZ dimensions in figure 11 indicated that the model was displaced by 0.034m, 0.076m and 0.011m respectively in the XYZ directions.

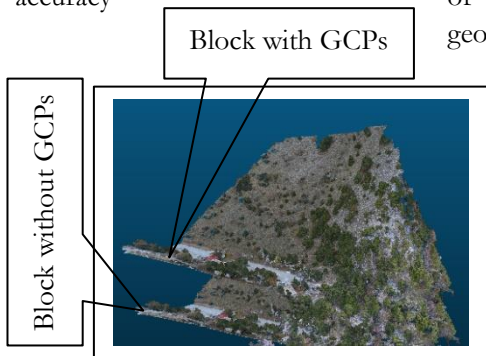


Figure 10: Shows the displacement of the image block

Absolute camera position and orientation uncertainties						
	X[m]	Y[m]	Z[m]	Omega [degree]	Phi [degree]	Kappa [degree]
Mean	0.016	0.020	0.017	0.038	0.008	0.034
Sigma	0.004	0.010	0.009	0.002	0.006	0.006

Absolute camera position and orientation uncertainties						
	X[m]	Y[m]	Z[m]	Omega [degree]	Phi [degree]	Kappa [degree]
Mean	0.094	0.096	0.164	0.049	0.058	0.067
Sigma	0.010	0.014	0.009	0.001	0.001	0.012

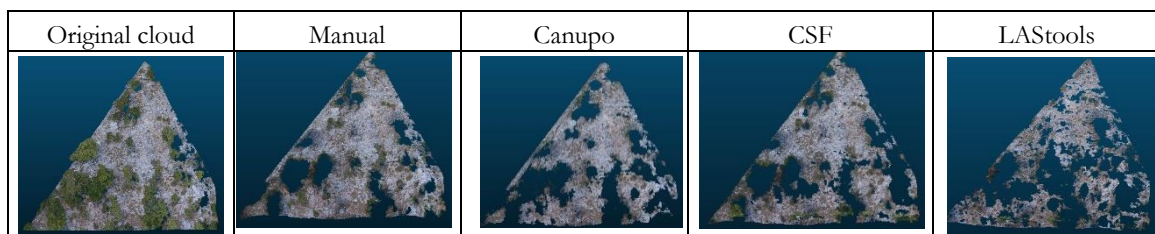
Figure 11: Quality report extract showing the differences in the XYZ dimensions between the 3D model with GCPs (above) and without GCPs (below) for the 2cm_GSD_45° model

Spatial accuracy differences in the two models leads to a conclusion that the model without GCPs gives unreliable spatial accuracy, hence is not ideal for parametric processing that requires accurate definition of the DFN for accurate interpretation of the discontinuity characterization. Hence, the datasets without GCPs were discarded while the georeferenced models were retained to be used in the subsequent stages of the research.

3.2.3. Vegetation removal methods

The three algorithms were unable to discriminate ground points from non-ground points (vegetation). The algorithms rely on the fixed height threshold from the terrain to separate non-ground points from ground points and in the process outcrops above this threshold were also removed. Similarly, low vegetation could not be removed due to the waviness of the slope terrain resulting in insignificant improvement in the quality of the data due to either presence of too much noise retained as residual vegetation or reduced point density due to excess removal of outcrops (Anders et al., 2019; Isenburg, 2014; Yilmaz et al., 2018; Zhang et al., 2016). Therefore, the data from the automated methods could not be used in the subsequent stages. Instead the data whose vegetation was removed manually vegetation used for further processing and analysis.

Table 4: Results of vegetation removal by different methods



Comparison between the automated methods, reveals that LAStools outperformed the other two automated methods as it removed the most vegetation in the point clouds evidenced by the small area covered by the residual vegetation after removal in relation to the total surface area of the point cloud as shown in figure 12 below. However, point density analysis of the 3D models after vegetation removal showed that LAStools significantly reduced the point density of the data by removing a substantial amount of ground points along with vegetation as evidenced by the results of the C2C distance computation in which the average point to point distance between the compared point cloud (LAStools) and the reference cloud (manual) is greater than the recommended zero (Girardeau-Montaut, 2015) as shown in appendix 2c while the results of CSF and CANUPO were satisfactory despite retaining a lot of residual vegetation in the datasets and also losing some terrain points especially the outcrops. Between the canupo and CSF, canupo performed relatively better than CSF as can be observed in table 5 and figure 12.

Table 5: Total areas covered by residual vegetation in each cloud after automatic vegetation removal

Method	2cm_Canupo	2.5cm_Canupo	2cm_CSF	2.5cm_CSF	2cm_LAStools	2.5cm_LAStools
Vegetation (m ²)	371	546	718	654	321	233
Model (m ²)	3446	3093	3418	3095	3432	3049

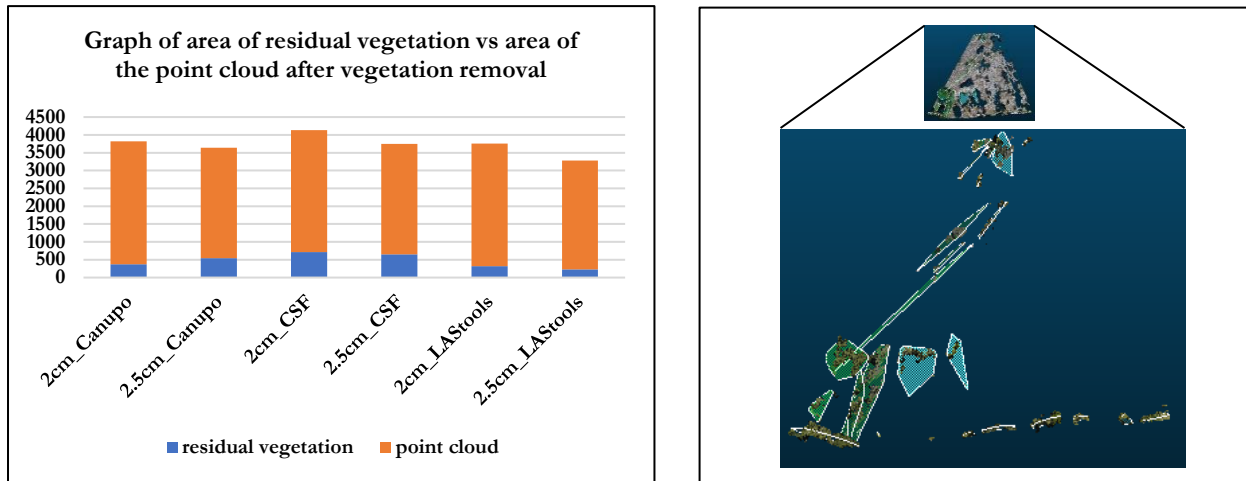


Figure 12: Surface areas covered by residual vegetation in a cloud (right) and plot of the area of the retained vegetation against the area of the cloud (left)

The surface area computation was done via segmentation of the residual vegetation parcels and then fitting a 2D polygon (facet) plane on the segments in cloudcompare. The procedure was repeated on the entire point cloud to calculate its surface area.

4. ROCK MASS DISCONTINUITY CHARACTERIZATION: SENSITIVITY TO PROCESSING PARAMETERS AND 3D MODEL SPATIAL RESOLUTION

4.1. Parametric processing

4.1.1. Methodology

To achieve sub objective 2 of the study, parametric processing of DSE parameters and spatial resolution sensitivity analysis of the UAV data was carried out to check the responses of each of the tested parameters

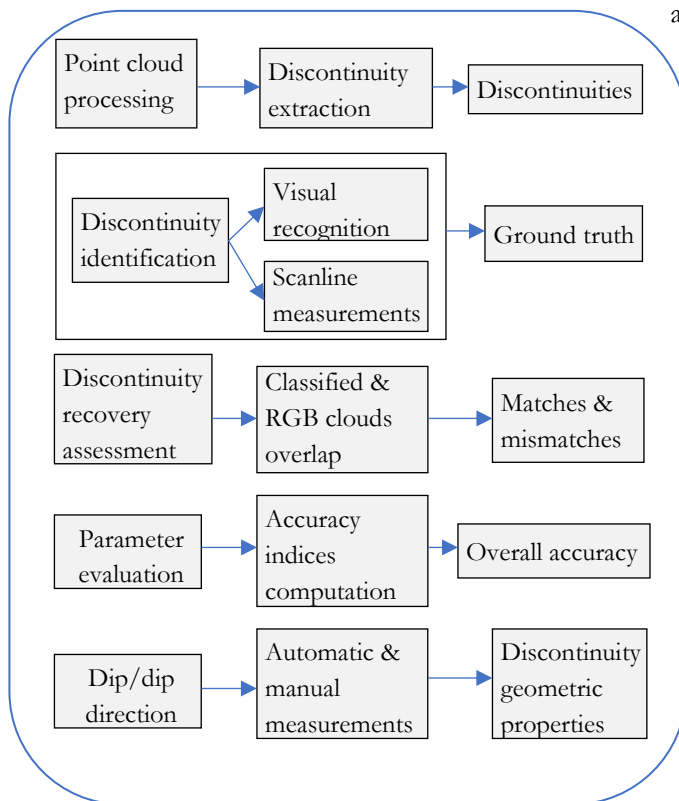


Figure 13: Methodology workflow

and the different resolution of the drone data on the discontinuity characterization of the rock mass of the study area. Figure 13 shows the summary of the workflow for the parametric processing.

4.1.1.1. Parameter selection and data

Parametric processing involved testing of a selected range of DSE parameter values during the processing of the data obtained from both the automated and manual UAV surveys on slope 1 & slope 2 respectively and checking the number of extracted discontinuities per discontinuity type and comparing the results between parameter values tested. Table 6 shows the selected parameters and the values that were tested during parametric processing. Parameter definitions are explained in table 7 below. The criteria for the parameter selection was based on ensuring that all the three steps of the discontinuity extraction in DSE i.e. curvature calculation and coplanarity test, statistical analysis and lastly clustering were

represented by at least one key parameter. On the other hand, the selection of the parameter values was based on the pre-trial check of the parameter response range from which the parameter value baselines were obtained as follows: **knn 30, α 10, β 30 and n_p 50**. The baseline parameter values were initial values for the parametric processing sensitivity tests. Each time a parameter value was tested, i.e. used during the extraction of the discontinuity sets by DSE, the other parameters were kept constant in order to check its response in terms of the number, type and the orientation of the discontinuities extracted and results compared to determine the optimal parameter value. The optimal parameter value was determined by visually checking the amount of overlap of the automatically extracted discontinuities with the manually extracted structures verified via ground truth data and computation of classification accuracy indices to check the effectiveness of the DSE in extracting the discontinuities at a particular parameter value. The matches and mismatches were subsequently used to determine the effectiveness of DSE to identify and extract discontinuities in a rock mass via the computation of overall accuracy.

Table 6: Selected DSE parameters for parametric processing

Parameter	Values tested
knn	5, 10, 20, 30, 40, 50, 60
α	5°, 10°, 15°, 20°, 30°, 40°, 50°
β	10°, 20°, 30°, 40°, 50°, 60°
n_p	30, 50, 100, 500, 1000

The GCP georeferenced data from slope 1 derived from the 36.3m perpendicular distance and camera tilt angle of 45° coded as 2cm_GSD model whose average point density was 682 points/m² or 5050 points/m³ and another dataset obtained from 45.3m perpendicular distance and camera tilt angle of 45° coded as 2.5cm_GSD model with

average point density of 382 points/m² or 2863 points/m³ representing the dataset obtained from the flight height of 58m of the automated surveys as indicated in table 1 and appendix 2 in addition to the dataset obtained from the manual flight on slope 2 whose average point density was 2018 points/m² or 18080 points/m³ were selected and used for this process. The selected datasets were preferred because they had higher relative point density necessary for the parametric processing to facilitate effective identification and extraction of the rock mass discontinuities in a point cloud. The extracted discontinuities were visualized in coudcompare.

4.1.1.2. Field measurements

Field measurements involved collection of onsite discontinuity data using scanline and geological compass. Two sections of slope 1 with some exposed outcrops were selected after a reconnaissance survey of the

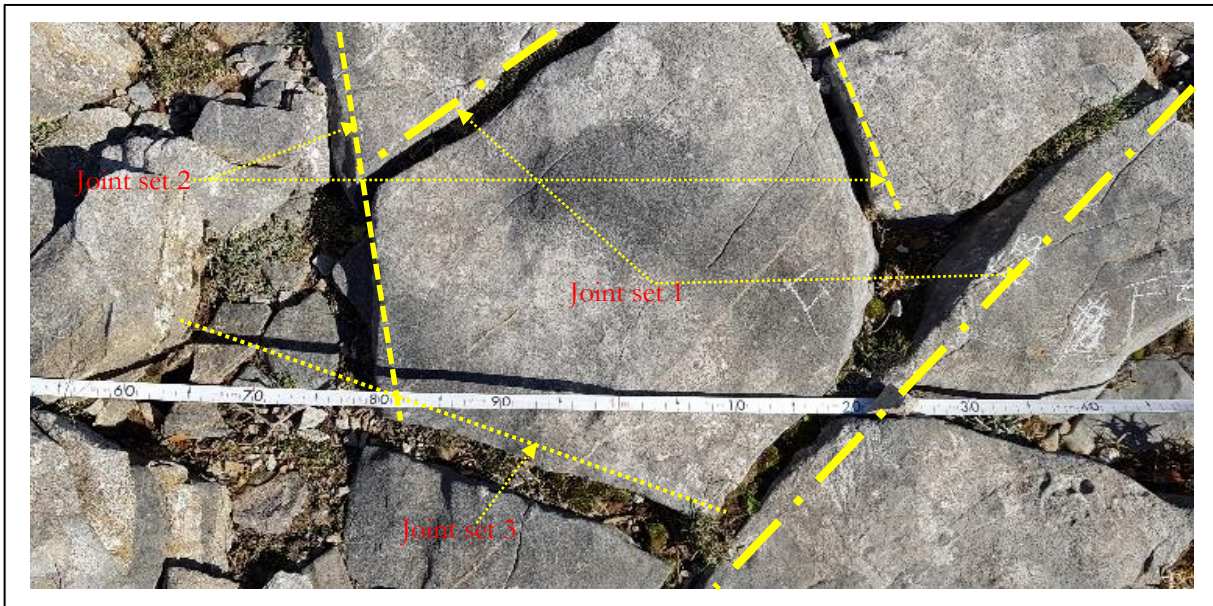


Figure 14: Scanline measurements

slope. Following the inspection, three discontinuity sets were identified and scanline measurements taken as shown in figure 14 above. The measurements obtained include: dip/dip direction, slope angle, joint aperture and spacing, persistence and Joint roughness coefficient as presented in appendix 4.

4.1.1.3. Parametric processing parameter definitions

Four principal parameters were selected for parametric processing namely: the **k-nearest neighbour (knn)** which denotes the number of neighbourhood points surrounding the seed or central point that DSE uses in conjunction with the tolerance parameter not discussed in this research to search for the coplanar or non-coplanar points based on the k value in order to set up planes; the minimum angle (α) between two normal vectors of 3D points in a point cloud, the maximum angle (β) between the normal vector of an assigned

point and the normal vector of the principal pole (central point) are the two angles DSE uses to compute the principal orientations of the plane and lastly, the number of points in a cluster (n_p) used by DSE during the clustering phase to determine the size of the clusters to be visualized in a plane. Table 6 explains the parameters used, their role during parametric processing and how they influence the results.

Table 7: Explains the parameters used in the parametric processing and how they influence the results

Parameter	Description	Influence of parameter changes on the results
knn	k-nearest neighbour denotes the number of neighbourhood points surrounding the seed or central point. k is the fixed number of neighbourhood points around the seed point. knn searches for the nearest neighbourhood points with similar features or homogenous characteristics depending on the value of k used during the local curvature calculation and coplanarity test to facilitate the setting up of planes (Riquelme et al., 2014; Vosselman & Maas, 2010).	Riquelme et al. (2014) concluded in their study that smaller knn retains a lot of noise in the data so as a compromise between resolution and accuracy the knn range of 15 – 30 was accepted. The point density of data the authors used however, is not stated therefore, not comparable to the resolution of the data used in this research.
α	This is the minimum angle between two normal vectors of 3D points in a point cloud. This angle is used by the algorithm statistical analysis method to calculate the principal orientation of the principal normal vectors. Principal orientation of the normal vectors determine the orientation of the planes for the discontinuities.	Wang et al. (2017) state that if the fracture is uneven (rough) then α should be large to allow the uneven structure grow into one region. Visual analysis and field data show that the discontinuity sets are relatively smooth therefore, the angle should be kept as small as practically possible. The implication is therefore, that results from the α parameter are influenced by roughness.
β	The maximum angle between the normal vector of an assigned point and the normal vector of the principal pole (central point) for a joint set. This is the angle the statistical method uses to check if a 3D point represents the principal orientation of the principal poles before it can be assigned to the principal pole.	If the local surface of the fracture has high roughness then β should be large to allow sufficient space for the small protrusions and dents in the fracture region (Wang et al., 2017). Visual analysis and field data show that the local surfaces of the discontinuity sets are highly undulated hence the angle should be kept as large as possible.
n_p	This is the minimum number of points in each cluster of a plane.	It depends on the size of clusters in each plane the user wishes to visualize (Riquelme et al., 2014). The smaller the n_p the smaller the size of the clusters and the larger the n_p the larger the clusters of the planes. To strike a balance between over-segmentation and under segmentation of the planes, $50 \leq n_p \leq 500$ range was adopted.

4.1.1.4. Discontinuity set identification and extraction in slope 1 and 2

Three main discontinuity sets were extracted from the dataset obtained from both the automated flight and manual flight data using DSE and visualized in cloudcompare based on the spectral information derived from the RGB camera to discriminate the discontinuities from the other objects (Spreafico et al., 2017). The discontinuity sets in the RGB point clouds were visually assessed and verified using an orthophoto. The automatically extracted sets results were checked against the visually assessed joint sets in the raw images in order to verify the correctness of the results. Figures 15 shows the visual recognition of the joint sets in an orthophoto from slope 1 whereas figure 16 shows the visually identified discontinuities in the slope 2 dataset.

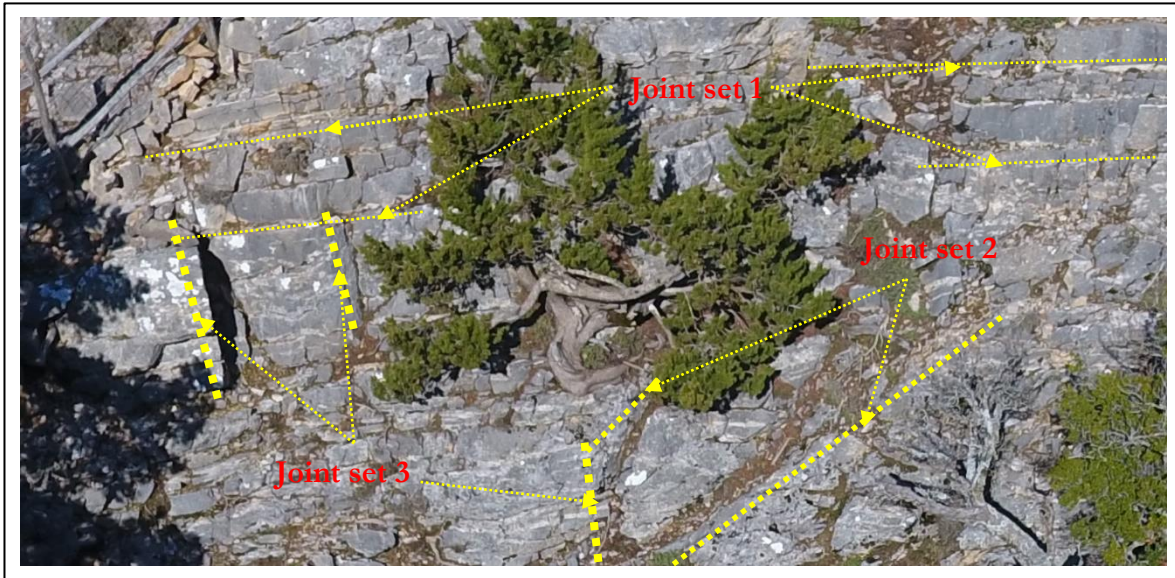


Figure 15: Visual recognition of joints in a raw image obtained from an automatic flight on slope 1

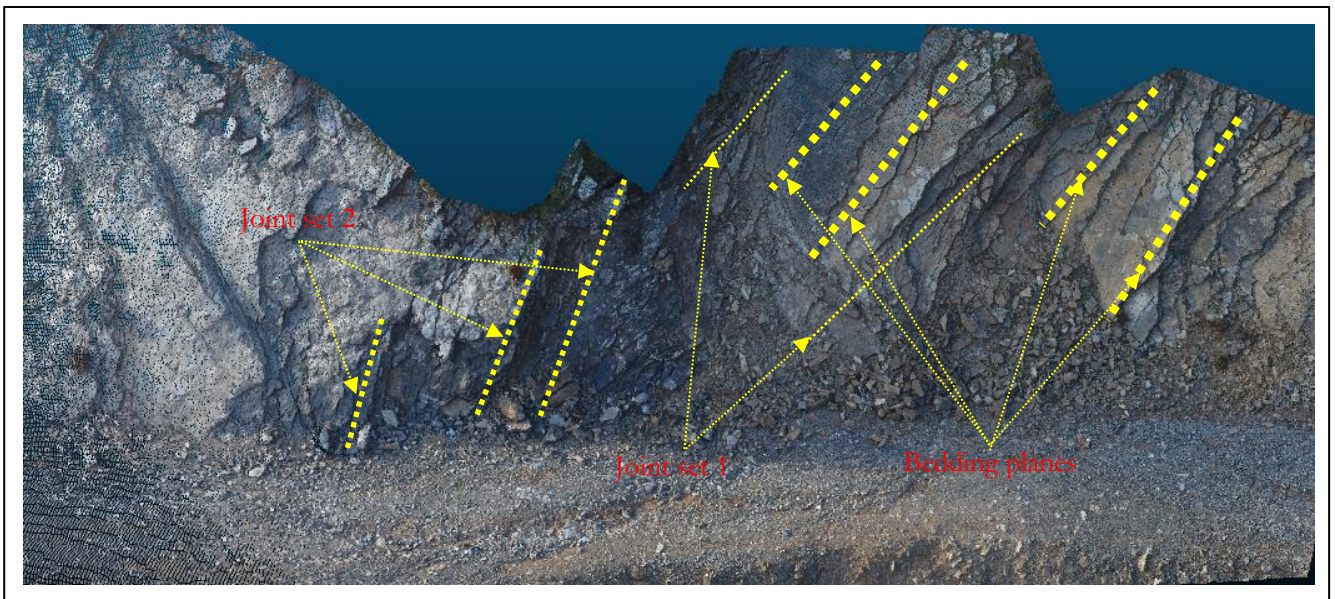


Figure 16: Visual recognition of the discontinuities in a raw image obtained from a manual flight on slope 2

4.1.1.5. Sensitivity analysis for the DSE processing parameters for slope 1 and 2

Grids were marked out on the RGB clouds for both automatic (2cm_GSD_45°, 2.5cm_GSD_45° models) and manual survey data to randomly sample the discontinuities after verification with the orthophoto. Inside the grid, ten (10) planar surfaces each belonging to joint set 1 (J1), joint set 2 (J2), and joint set (J3) were selected and labelled with the alphanumeric characters in the distinctive colours to distinguish one set from the other as shown in figures 17, 18 and 19. After each execution of the DSE parameter value test, the results of the discontinuity extraction in the classified point cloud were overlaid against the RGB cloud to check the overlap of the extracted discontinuities with the corresponding sets within the sampled grid to verify the correctness of the results. The overlap results were used to compute the accuracy indices for each parameter value tested to quantitatively evaluate the effectiveness of each experimental parameter value during the recovery of the geological structures. The accuracy indices computed include overall accuracy, producer accuracy (PA), user accuracy (UA), error of omission (OE) and error of commission (CE). The overall accuracy measured the effectiveness of the DSE to extract the discontinuities at pre-set parameter values while PA represented how well the discontinuity sets were identified by the software and UA indicated the reliability or probability of DSE to correctly predict the discontinuity sets in a rock mass. On the other hand, the CE showed the proportion of the discontinuities that were incorrectly predicted or false alarms by DSE and OE indicated the missed alarms or the proportion of the discontinuities that were not identified by DSE (Spreafico et al., 2017). The following equations were used to compute overall accuracy, PA, UA, OE and CE (Banko, 1998; Story & Congalton, 1986):

$$\text{Overall accuracy} = \text{total of all correctly identified discontinuities} / \text{total of all sampled discontinuities} \dots (1)$$

$$\text{PA} = \text{total of correctly identified discontinuity set} / \text{total of discontinuity set (column total)} \dots\dots\dots(2)$$

$$\text{UA} = \text{total of correctly predicted discontinuity set} / \text{total of predicted set (row total)} \dots\dots\dots(3)$$

$$\text{OE} = \text{total of incorrectly identified discontinuity set} / \text{total of discontinuity set (column total)} \dots\dots\dots(4)$$

$$\text{CE} = \text{total of incorrectly predicted discontinuity set} / \text{total of predicted set (row total)} \dots\dots\dots(5)$$

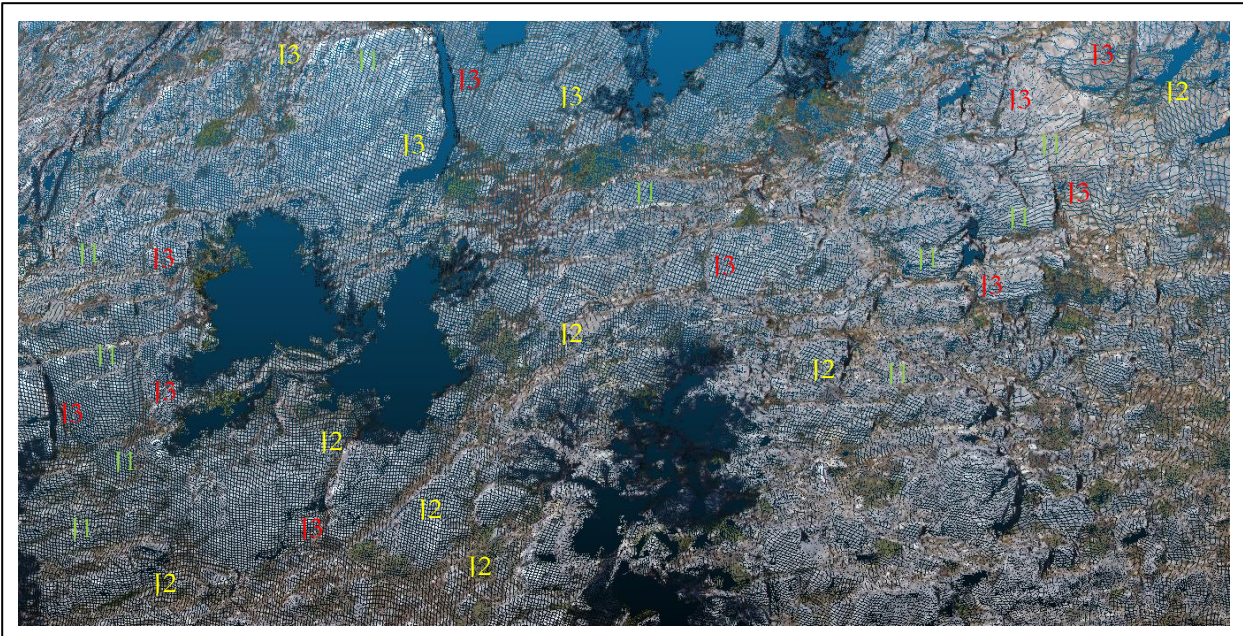


Figure 17: Selected joint sets within the selected grid on the RGB cloud of the 2cm_GSD_45° data from slope 1

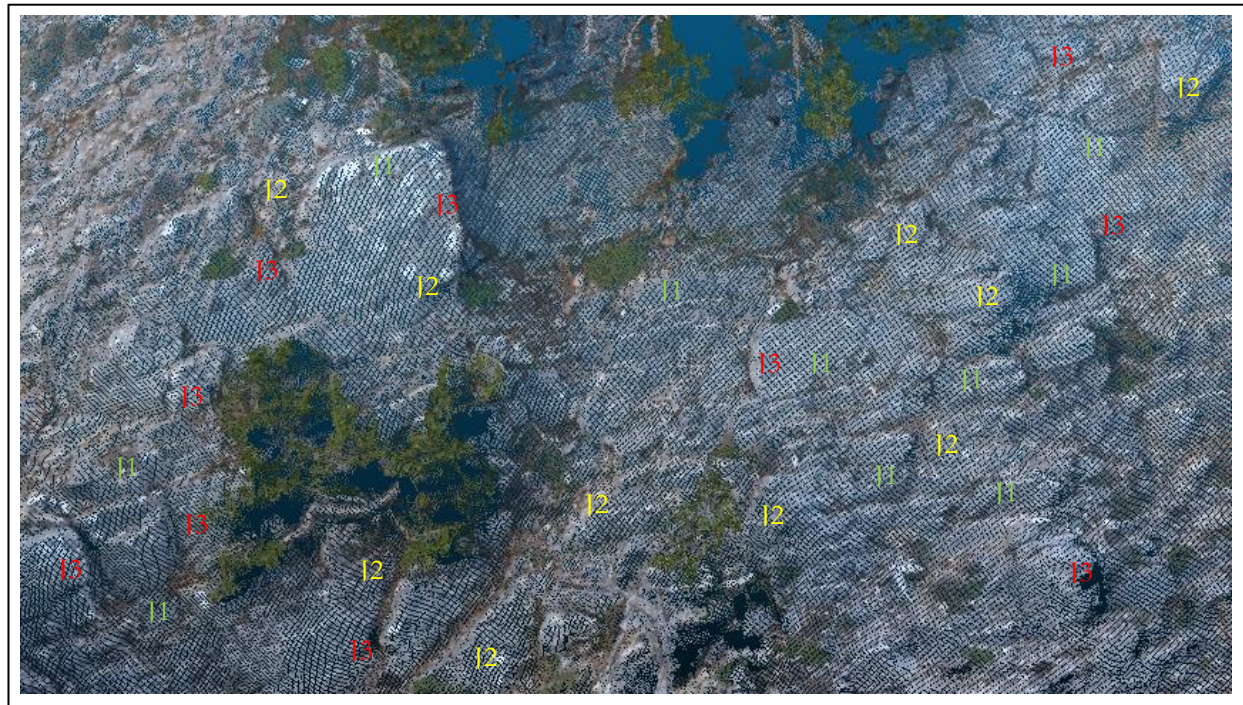


Figure 18: Sampled joints within the selected grid on the RGB cloud of the 2.5cm_GSD_45° data from slope 1

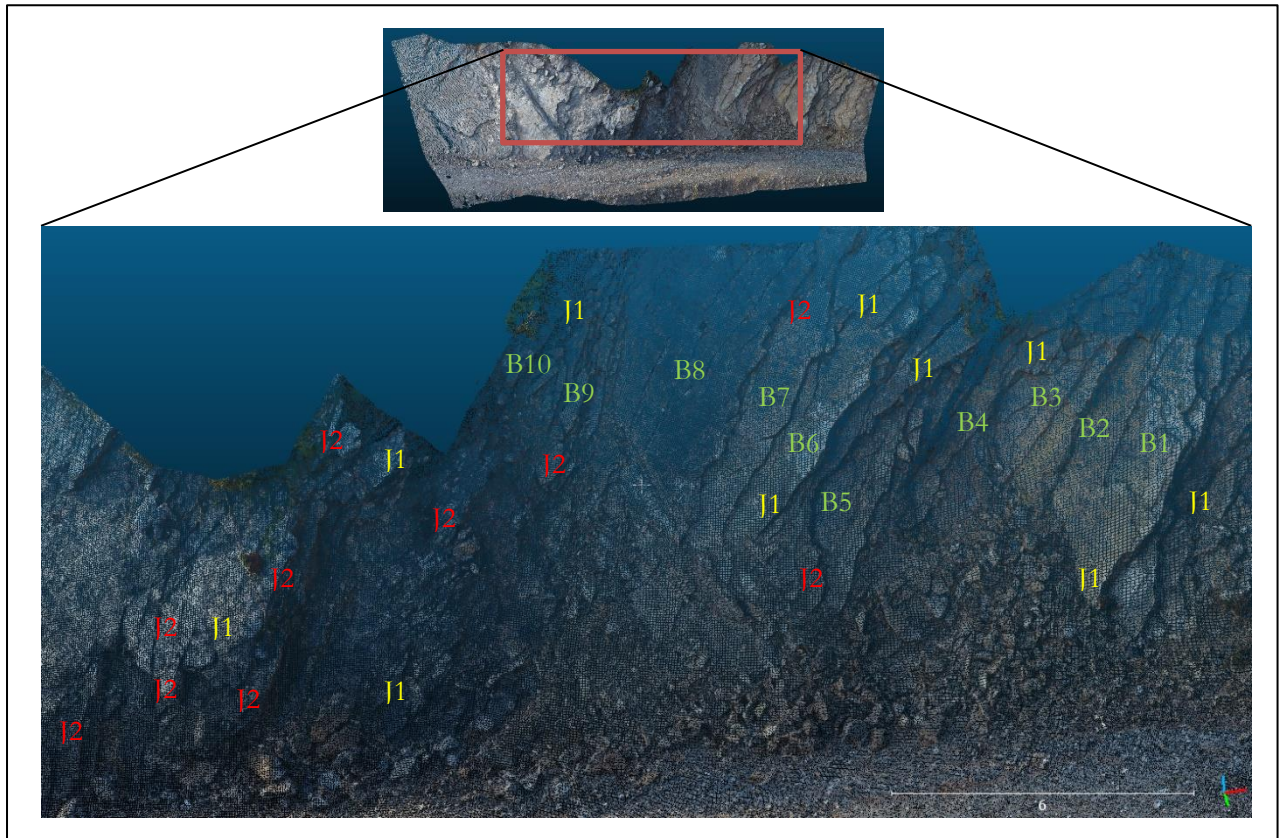


Figure 19: Location of the sampled discontinuity sets within the selected grid on the RGB cloud of slope 2 data

4.1.1.6. Orientation measurements for the discontinuities

In addition, to the field measurements, the joint sets dip/dip direction values were automatically obtained from the **stereoplots** of the DSE statistical analysis results and also manually extracted from the two point clouds (2cm_GSD_45°) and (2.5cm_GSD_45°) via the **compass tool** in cloudcompare. However, due to too many undulations on slope 1 surface, manual extraction of the attitude of the of the discontinuity sets was cumbersome, hence the individual sample results were inconsistent. Therefore, ten attitude values were randomly obtained from each extracted set and averaged. Manual recovery of the orientation values was also executed on the slope 2 data. One set of the results from each of the two point clouds was selected and used to plot a stereograph using an online interactive stereonet App called **visiblegeology**.

4.1.2. Analysis and Results

4.1.2.1. Slope 1

The automatic discontinuity extraction results from the slope 1 data were generally poor across all the four parameter tested. The poor results were attributed to the presence of noise in the data due to presence of

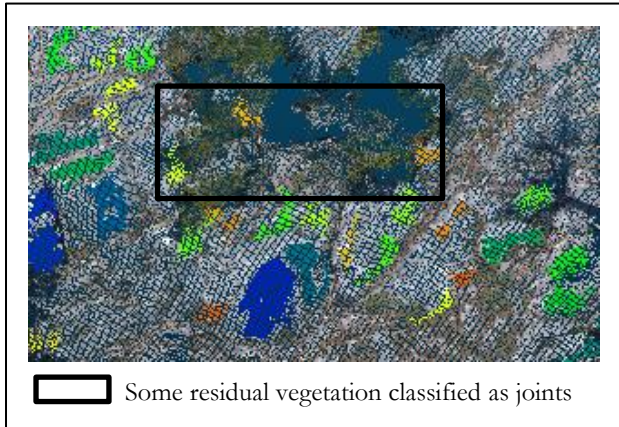


Figure 20: Poor results due to noise

low vegetation, residual vegetation from the vegetation removal process, shadowing effect from the higher vegetation, occlusions, lack of sufficient exposed rock mass surfaces and too many undulations on the slope surface. Figure 20 shows an extract of poor results in a classified cloud. However, qualitative analysis of the results showed some improvement after increasing the number of points in each cluster of a plane (n_p) from 50 to 500 during the clustering stage in order to suppress some noise for each parameter run as illustrated in figure 21.

The presence of the noise and other spurious objects in the data contributed to the over segmentation of the planes of the structures which included the noise itself. This is consistent with the findings of (Riquelme et al., 2014; Vosselman & Maas, 2010). In addition to suppressing the noise, increasing n_p made visualization of the overlap results better. However, making n_p too large had some drawbacks. Considering that the geology of the study area is predominantly platy limestones with very tiny spacing in the order of 10cm

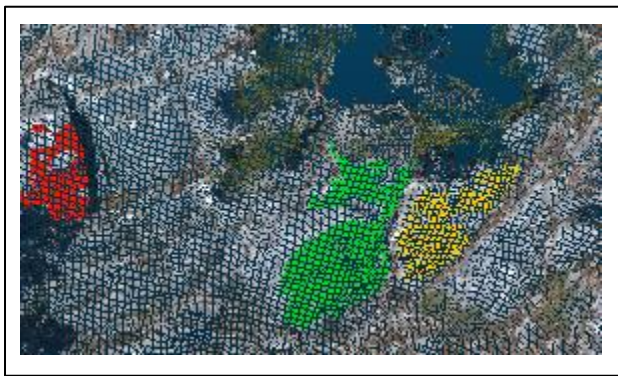


Figure 21: Improved results after increasing n_p

confirmed by measurements on the point cloud and scanline measurements, small joint sets could not be extracted due to under segmentation of the planes resulting in reduced number of some discontinuities observed especially J2 and J3 since they are deep seated into the rock mass and are fewer in number compared to J1. The reduction in the number of the recovered geological structures resulted in low classification overall accuracies as shown in the tables presented in appendices 3a, 3b and 3c.

Analysis of the accuracy indices showed a fluctuating trend in the results when changing the knn values and keeping α , β and n_p fixed at 10° , 30° and 500 respectively as shown in appendix 3a and 3b. On the other hand, varying α and keeping knn constant at 30, β at 30° and n_p at 500 generally revealed a linear trend in the results in which better results were obtained at lower values of α while in the β experiments, better results were obtained at higher values of β as presented in appendix 3a and 3b when knn, α and n_p were fixed at 30, 10° and 500 respectively. The accuracy indices results also showed the algorithm consistently extracted more J1 than any other joint sets across all the tested parameter values.

Further, the results of the computed accuracy indices for each of the tested parameter values showed that the highest overall accuracies for the three parameters keeping other parameters constant on the 2cm_GSD_45° data during each individual parameter value test, were achieved at **knn 10**, **$\alpha 15^\circ$** and **$\beta 50^\circ$** as shown in tables 8, 9 and 10. The highest overall accuracy in the knn parameter value tests while keeping α fixed at 10° , β at 30° and n_p at 500 was observed to be **40%** corresponding to knn 10. This overall accuracy

implied that the effectiveness of DSE to optimally identify and extract all the three sets of the discontinuities was 40%. The software however, correctly recognized individual joints with 90% for J1, 30% for J2 and 0% for J3 accuracy. A much improved proportionate extraction of discontinuities for all the three joint sets was observed at knn 40 with the following extraction distributions: 60% for J1, 20% for J2 and 10% for J3 despite the low overall accuracy as shown in appendix 3a.

Table 8: Confusion matrix for the discontinuity overlap classification accuracy indices at knn₁₀

		Actual					Accuracy indices (%)			
		J1	J2	J3	NO	Total	CE	OE	UA	PA
Predicted	J1	9	7	6	0	22	59.09	10	40.91	90
	J2	1	3	2	0	6	50	70	50	30
	J3	0	0	0	0	0	0	100	0	0
	NO	0	0	2	0	2	100	0	0	0
	Total	10	10	10	0	30	Overall Accuracy (%)			40

Further scrutiny of the computed accuracy indices, showed that the highest overall accuracy for the α tests of different parameter values and keeping knn, β and n_p fixed at 30, 30° and 500 respectively was achieved at **40%** corresponding to α 15° as shown in table 9 below. This indicated that on average, DSE effectiveness to recognize and extract discontinuities in a rock mass was **40%**. The algorithm however, successfully identified and extracted the sampled individual discontinuities with the following accuracies: 80% of the J1, 30% for J2 and 10% for J3.

Table 9: Confusion matrix for the discontinuity overlap classification accuracy indices at α_{15}

		Actual					Accuracy indices (%)			
		J1	J2	J3	NO	Total	CE	OE	UA	PA
Predicted	J1	8	7	5	0	20	60	20	40	80
	J2	2	3	2	0	7	57.14	70	42.86	30
	J3	0	0	1	0	1	0	90	0	10
	NO	0	0	2	0	2	100	0	0	0
	Total	10	10	10	0	30	Overall Accuracy (%)			40

In the β parameter value tests while maintaining knn, α and n_p fixed at 30, 10° and 500 the highest overall accuracy achieved was **47%** corresponding to β 50° as shown table 10. The overall accuracy results showed that the effectiveness of DSE to optimally identify and extract the three joint sets was **47%**. Nonetheless, the software correctly identified and extracted individual discontinuities with the following accuracies: 80% for J1, 20% for J2 and 40% for J3.

Table 10: Confusion matrix for the discontinuity overlap classification accuracy indices at β_{50}

		Actual					Accuracy indices (%)			
		J1	J2	J3	NO	Total	CE	OE	UA	PA
Predicted	J1	8	7	5	0	20	60	20	40	80
	J2	2	2	1	0	5	60	80	40	20
	J3	0	1	4	0	5	20	60	80	40
	NO	0	0	0	0	0	0	0	0	0
	Total	10	10	10	0	30	Overall Accuracy (%)			46.67

Similarly, varying the three separate test parameters and keeping other parameters fixed during the extraction of the discontinuities from the 2.5cm_GSD_45° data achieved the highest overall accuracies at **knn 30, α 15° and β 40°** respectively as tabulated in tables 11, 12 and 13. Varying knn parameter values and keeping α , β and n_p constant at 10°, 30° and 500 constant throughout the parameter experiments achieved the highest overall accuracy of **33%** implying that on average, DSE only effectively identified and extracted 33% of the sampled three joint sets. This overall accuracy corresponded to knn 30. Also, DSE correctly identified individual discontinuities with up to 90% of J1, 10% of J2 and 0% of J3 accuracy.

Table 11: Confusion matrix for the discontinuity overlap classification accuracy indices at knn₃₀

		Actual					Accuracy indices (%)				
		J1	J2	J3	NO	Total	CE	OE	UA	PA	
Predicted	J1	9	9	8	0	26	65.38	10	34.62	90	
	J2	1	1	1	0	3	0	90	0	10	
	J3	0	0	0	0	0	0	100	0	0	
	NO	0	0	1	0	1	0	0	0	0	
	Total	10	10	10	0	30	Overall Accuracy (%)			33.33	

Further, changing α values and keeping knn, β and n_p fixed at 30, 30° and 500 respectively achieved the highest overall accuracy of **37%** corresponding to α 15° as shown in table 12 below. This revealed that on average, DSE effectiveness to recognize and extract discontinuities in a rock mass was **37%**. The algorithm however, successfully identified and extracted the sampled individual discontinuities with the following accuracies: 90% of the J1, 20% for J2 and 0% for J3.

Table 12: Confusion matrix for the discontinuity overlap classification accuracy indices at α_{15}

		Actual				Accuracy indices (%)				
		J1	J2	J3	NO	Total	CE	OE	UA	PA
Predicted	J1	9	8	8	0	25	64	10	36	90
	J2	1	2	2	0	5	60	80	40	20
	J3	0	0	0	0	0	0	100	0	0
	NO	0	0	0	0	0	0	0	0	0
	Total	10	10	10	0	30	Overall Accuracy (%)			36.67

Lastly, varying β values and maintaining knn, α and n_p fixed at 30, 10° and 500 achieved the highest overall accuracy of **40%** corresponding to β 40°, β 50° and β 60° as tabulated in table 13 and appendix 3b. This showed that the effectiveness of DSE to optimally identify and extract the three joint sets was 40%. Nevertheless, DSE correctly identified and extracted individual discontinuities with the following accuracies: 90% for J1, 30% for J2 and 0% for J3.

Table 13: Confusion matrix for the discontinuity overlap classification accuracy indices at β_{40}

		Actual				Accuracy indices (%)				
		J1	J2	J3	NO	Total	CE	OE	UA	PA
Predicted	J1	9	7	8	0	24	62.5	10	37.5	90
	J2	1	3	2	0	6	50	70	50	30
	J3	0	0	0	0	0	0	100	0	0
	NO	0	0	0	0	0	0	0	0	0
	Total	10	10	10	0	30	Overall Accuracy (%)			40

4.1.2.2. Slope 2

Unlike the results from slope 1, slope 2 results were generally satisfactory across the four parameters. The results of overlap between the extracted discontinuities in the classified cloud and the RGB cloud correlated well as shown in the example in figure 22. The good results were attributed to the noise free data from slope 2, sufficient exposure of the rock mass surface and absence of extreme undulated surfaces on the slope.

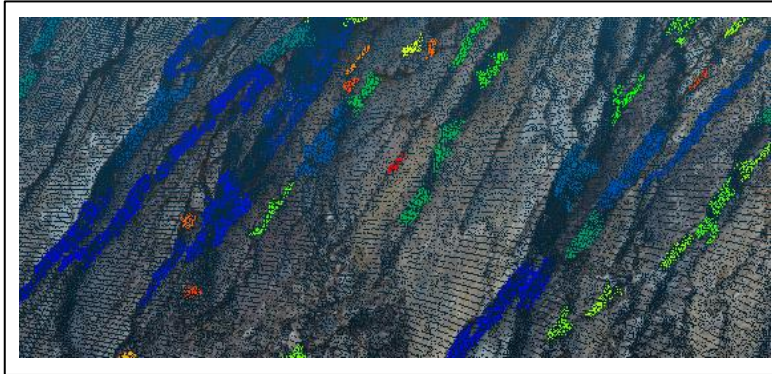


Figure 22: Extract of the results of overlap between the joints in the classified and the RGB clouds

Similar to the results obtained from slope 1, closer inspection of the structures overlap results between the discontinuities in the classified and RGB point clouds generally showed that the bedding planes (Bs) were extracted more than J1 and J2. The n_p 50 produced better results and was therefore, maintained fixed at 50 in all the experiments.

Evaluation of the tested parameters revealed a trend in the results consistent with the findings in slope 1 where variations in the knn values and maintaining α , β and n_p constant at 10° , 30° and 50 respectively

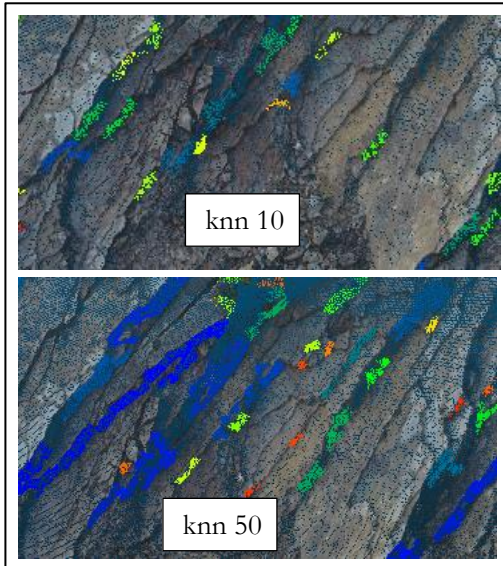


Figure 23: Results of discontinuity set overlap at different knn values

produced fluctuating results as presented in appendix 3c. Fluctuating results, mean that the overlap results did not show a linear trend across the tested knn values. Figure 23 shows the results of overlap of the joint sets between the classified cloud and the RGB cloud at different knn values. Conversely, when α was varied and knn, β and n_p were kept constant at 30, 30° and 50 generally produced results that showed a linear trend in which better results were obtained at lower values of α while in the β experiments, better results were obtained at higher values of β when knn, α and n_p were fixed at 30, 10° and 50 respectively as presented in appendix 3c. The accuracy indices also showed that the algorithm consistently extracted more Bs than any other discontinuity sets across all the tested parameter values.

The computed accuracy indices for each of the tested parameter values further showed that the highest overall accuracies for the three parameters keeping other parameters constant on slope 2 data during each individual parameter value test, were achieved at **knn 40**, α 15° and β 50° as shown in tables 14, 15 and 16. The highest overall accuracy in the knn parameter value tests while keeping α fixed at 10° , β at 30° and n_p at 50 was observed to be **73%** which implied that the effectiveness of DSE to optimally identify and extract all the three sets of the discontinuities was **73%** if knn is set to 40 and keeping α , β and n_p constant at 10° , 30° and 50 respectively. Further, the software correctly recognized individual joints with an accuracy of 70% for the Bs, 80% for J1 and 70% for J2 as shown in table 14 below.

Table 14: Confusion matrix for the discontinuity overlap classification accuracy indices at knn_{40}

		Actual				Accuracy indices (%)				
		B	J1	J2	NO	Total	CE	OE	UA	PA
Predicted	B	7	2	2	0	11	36.36	30	63.64	70
	J1	2	8	1	0	11	27.27	20	72.73	80
	J2	1	0	7	0	8	12.5	30	87.5	70
	NO	0	0	0	0	0	0	0	0	0
	Total	10	10	10	0	30	Overall Accuracy (%)			73.33

Analysis of the computed accuracy indices for the α value tests, showed that the highest overall accuracy of 80% was achieved when knn , β and n_p were fixed at 30, 30° and 50 respectively corresponding to α 15° as shown in table 15 below. This result indicated that on average, DSE effectiveness to recognize and extract discontinuities in a rock mass was **80%**. The algorithm, successfully and correctly identified and extracted the sampled individual discontinuities with the following accuracies: 80% of the Bs, 90% for J1 and 70% for J2.

Table 15: Confusion matrix for the discontinuity overlap classification accuracy indices at α_{15}

		Actual				Accuracy indices (%)				
		B	J1	J2	NO	Total	CE	OE	UA	PA
Predicted	B	8	0	1	0	9	11.11	20	88.89	80
	J1	2	9	1	0	12	25	10	75	90
	J2	0	1	7	0	8	12.5	30	87.5	70
	NO	0	0	1	0	1	0	0	0	0
	Total	10	10	10	0	30	Overall Accuracy (%)			80

Variations in the β parameter values while keeping knn , α and n_p fixed at 30, 10° and 50 the highest overall accuracy achieved was **73%** corresponding to β 50° and β 60° as shown table 16 and appendix 3c. This result showed that the effectiveness of DSE to optimally identify and extract the three discontinuity sets was 73%. Further, the software correctly identified and extracted individual sampled discontinuities with the following accuracies: 100% for Bs, 80% for J1 and 40% for J2.

Table 16: Confusion matrix for the discontinuity overlap classification accuracy indices at β_{50}

		Actual				Accuracy indices (%)				
		B	J1	J2	NO	Total	CE	OE	UA	PA
Predicted	B	10	0	3	0	13	23.08	0	76.92	100
	J1	0	8	0	0	8	0	20	0	80
	J2	0	2	4	0	6	33.33	60	66.67	40
	NO	0	0	3	0	3	0	0	0	0
	Total	10	10	10	0	30	Overall Accuracy (%)			73.33

4.1.2.3. Comparison of the overall accuracies between slope 1 & 2

Comparison of the overall accuracies computed for the slope 1 and slope 2 data shows that slope 2 data outperformed the data from slope 1 in all the parameters as shown in figures 24, 25 and 26 below. As illustrated in figure 24, the peaks in the knn parameter tests results were: in slope 1, the 2cm_GSD_45° model peaks at knn 10 and the 2.5cm_GSD_45° model the knn peak is at the value of 30. On the other hand, slope 2 peaks at knn 40. Further comparison between the slope 1 datasets revealed that the 2cm_GSD_45° model generally produced higher overall accuracies than the 2.5cm_GSD_45° model a confirmation that higher point density data performed better than the lower point density datasets.

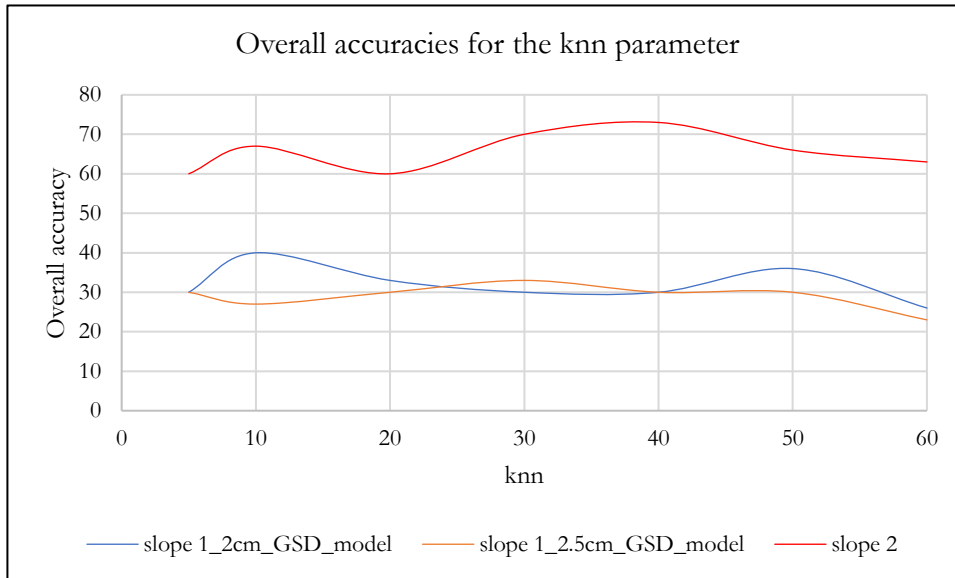


Figure 24: Overall accuracies for the knn parameter on slope 1 & 2 data

Similarly, figure 25 below shows that in the α experiments, the peaks in both slope 1 and slope 2 data were at α 15. However, in the β parameter experiments, the peaks for the 2cm_GSD_45° and 2.5cm_GSD_45° models were observed at β 50°, β 60° and β 40°, β 50°, β 60° respectively whereas for slope 2 data the peak was observed at β 50°, β 60° as indicated in figure 26.

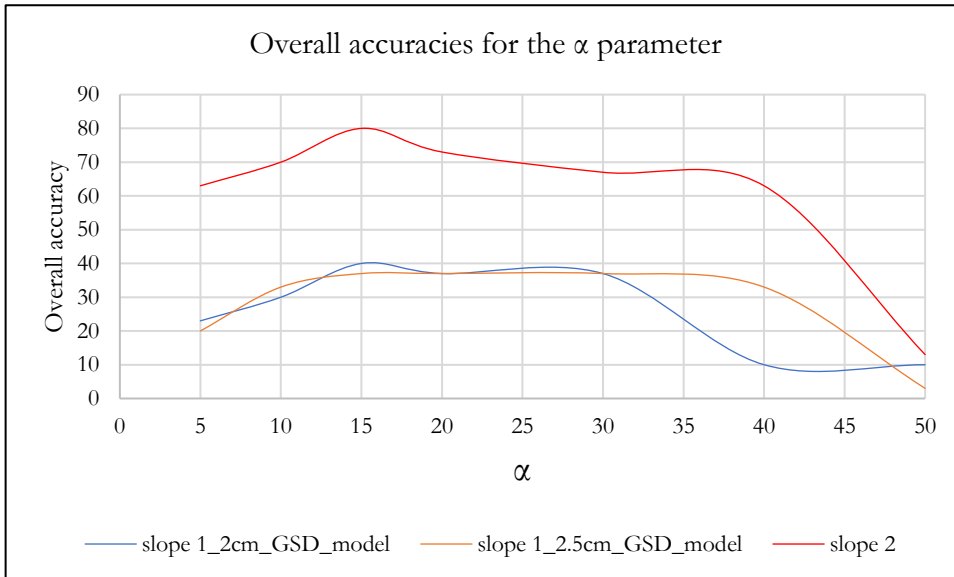


Figure 25: Overall accuracies for the α parameter on slope 1 & 2 data

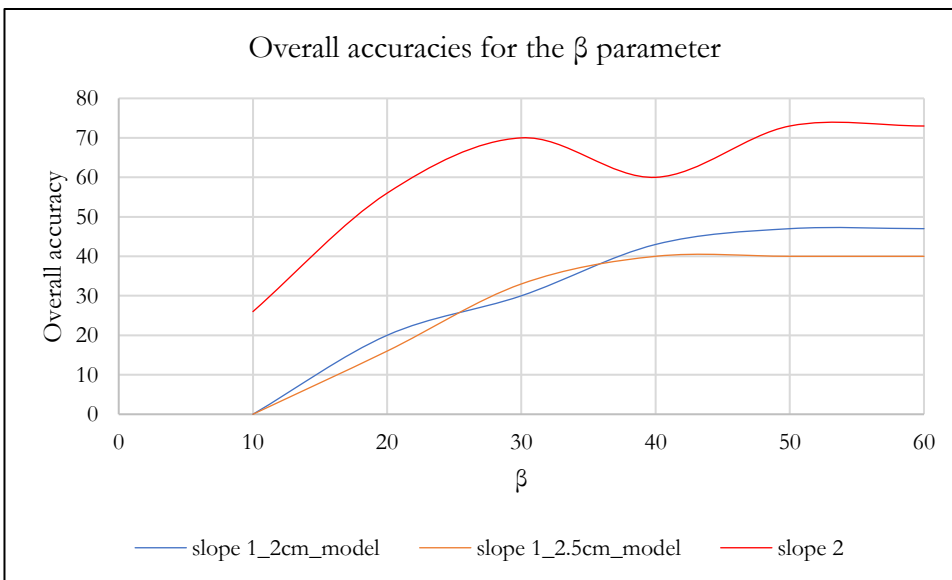


Figure 26: Overall accuracies for the β parameter on slope 1 & 2 data

4.1.2.4. Orientation of the joint sets

The analysis of the geometrical properties of the joint sets in slope 1 data depicted in the clouds generally showed a consistent trend in dip and dip direction. Figures 27 and 28 below show examples of the orientation of the discontinuities extracted from the automated flight data by varying knn parameter while keeping the other parameters fixed. Tables 17 and 18 show the comparison of the dip/dip direction results between the automatically extracted dip/dip direction values via the stereoplot of the DSE and manual extraction from the classified point using a picking tool in cloudcompare. It was observed that J2 and J3 have larger dip angles compared to J1 an indication that J2 and J3 are sub vertical structures whereas J1 is horizontal. Extra checks reviewed that there was slight shift in the orientation of J3 between the two models in the two scenarios. The trend was similar with slope 2 data. The bedding planes were observed to be horizontal and J1 and J2 sub vertical.

Table 17: Examples of Dip/dip direction of the joints extracted when knn values were varied while keeping others constant on the 2cm_GSD model with GCPs.

Experiment	Orientation						Comment
	Manual			Automatic			
knn	J1	J2	J3	J1	J2	J3	
10	46/177	85/337	83/353	44/177	88/344	88/30	Planes with smaller densities were discarded as noise (uncertainties) in the data because large differences in densities affect the automatic extraction of the joint sets (Ester et al., 1996; Lato et al., 2010)
20	48/166	79/329	83/354	44/177	89/342	0	
30	50/179	82/326	80/350	44/177	89/342	89/353	
40	54/179	81/332	83/355	44/177	89/342	89/353	
50	50/182	81/326	83/355	44/177	89/342	0	
60	46/177	85/337	83/353	44/177	89/342	89/359	

Table 18: Examples of Dip/dip direction of the joint sets recovered when knn was varied while keeping other parameters fixed on the 2.5cm_GSD model with GCPs

Experiment	Orientation						Comment
	Manual			Automatic			
knn	J1	J2	J3	J1	J2	J3	
10	47/178	81/334	83/356	49/183	87/338	89/356	Planes with smaller densities were discarded as noise (uncertainties) in the data because large differences in densities affect the automatic extraction of the joint sets (Ester et al., 1996; Lato et al., 2010)
20	54/169	82/336	81/354	49/171	89/342	89/356	
30	48/175	82/336	nil	49/183	87/338	0	
40	50/172	82/331	79/356	49/171	88/335	89/356	
50	54/165	82/333	82/356	50/165	88/335	89/356	
60	53/185	81/328	80/350	49/183	87/338	89/356	

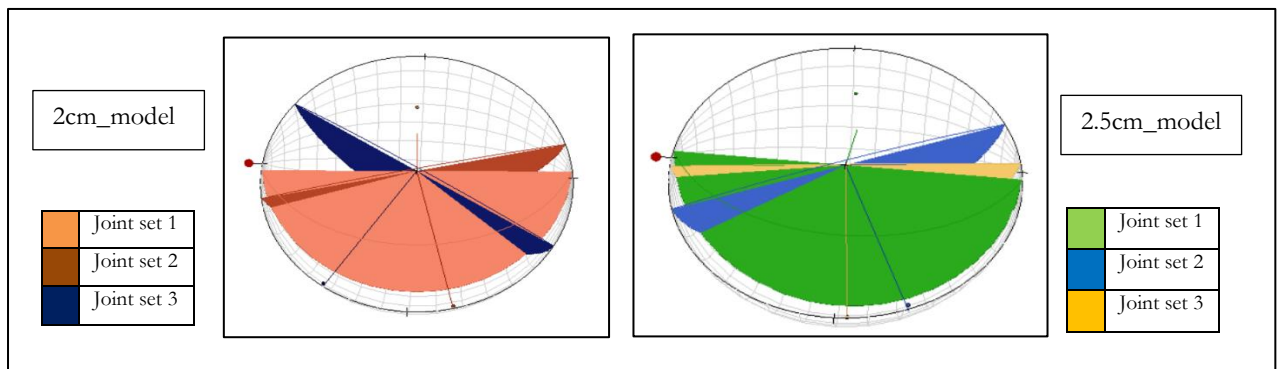


Figure 27: Stereographic projection showing the dip/dip directions of the joint sets automatically identified

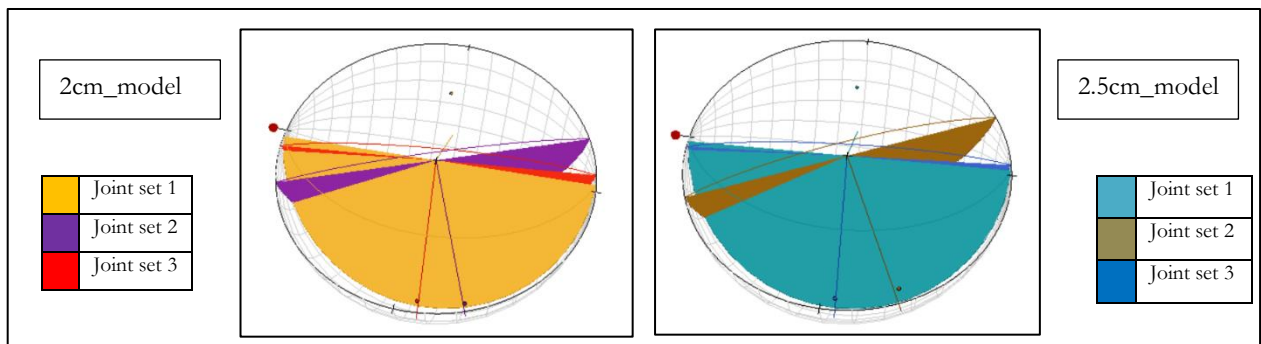
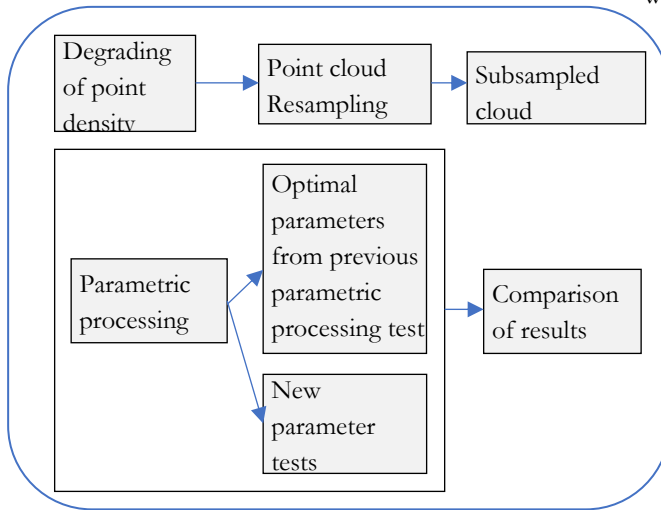


Figure 28: Stereographic projection showing the dip/dip directions of the joints manually recognized

4.2. Spatial resolution sensitivity

4.2.1. Methodology

To further answer the research sub objective 2, spatial resolution sensitivity test was carried out on the downgraded point cloud that involved subsampling of the slope 2 data eight (08) times to progressively reduce its point density and intuitively check the response of the downgraded point density data to the automatic discontinuity set extraction procedure. The data was resampled at the intervals of 5cm of the minimum space between points beginning with the 5cm and ending with 50cm. The downgraded datasets



were subsequently subjected to the automatic discontinuity set extraction in DSE using the optimal parameter values derived from the previous parametric processing procedure. The optimized parameter values were **knn 40, α 15° and β 50°**. After the extraction of the geological structures, the classified point clouds were overlaid on the RGB cloud in order to progressively fit planes to the structures and also point densities of the tested clouds checked using cloudcompare. The experiments were repeated until no more structures could be extracted by DSE in the resampled cloud at which it was recorded as a tipping point.

Figure 29: Methodology workflow

4.2.2. Analysis and Results

Analysis of the results in table 19 below revealed a proportional reduction in the point density of the discontinuities recovered in each of the resampled point cloud. Further scrutiny of the results showed that **43 points/m²** flagged red was the minimum point density required to enable extraction of the discontinuity sets beyond which it was impossible to extract any more discontinuities and instead began to introduce some noise in the results as shown in the 25cm and 30cm results figure 30.

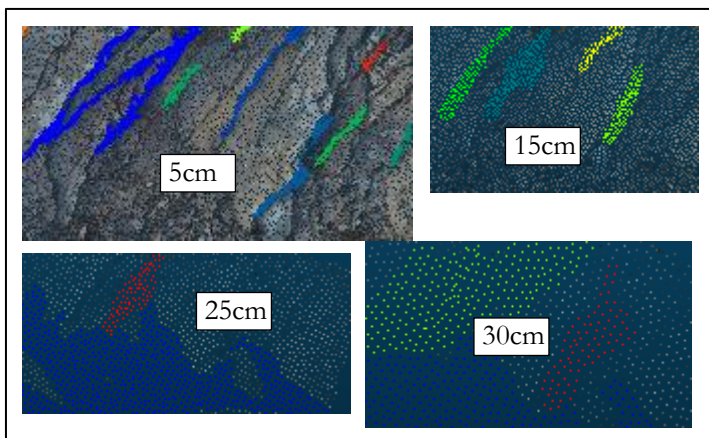


Figure 30: Results of joints overlap in the subsampled classified and RGB clouds at optimal parameter values

Table 19: Densities of subsampled clouds

Minimum distance between points (cm)	Point density (pts/m ²)
5	531
10	149
15	72
20	43
25	29
30	17
40	8
50	5

Qualitative analysis, showed that changing the knn value from 40 to 50 and keeping the α , β and n_p fixed at 15° , 50° and 50 respectively improved the amount of extracted discontinuities as illustrated in figure 31. Similarly, α and β values were varied from 15 and 50 respectively to $\alpha 10^\circ$, $\alpha 5^\circ$ and $\beta 40^\circ$, $\beta 30^\circ$ while knn was kept fixed at 40 and n_p at 50. The visual inspection of the structures overlap results in the classified and RGB clouds confirmed that there was no significant change in the results with respect to the results obtained

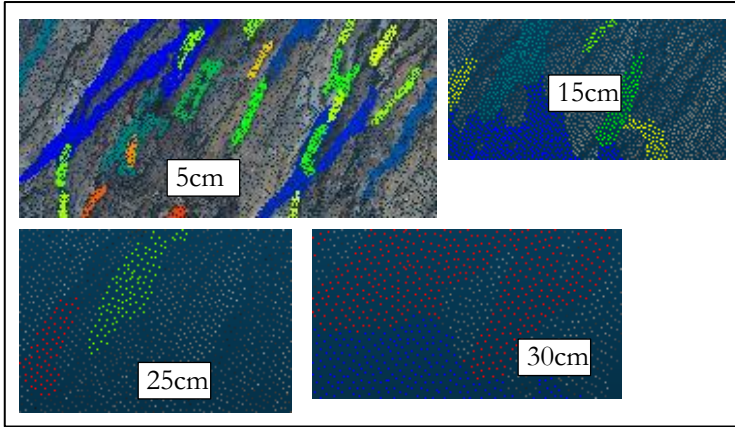


Figure 31: Results of joints overlap in the subsampled classified and RGB clouds at knn 50 and constant α , β and n_p

changed from 43 pts/m² to 149 pts/m² which corresponded to the 10cm point spacing in the cloud beyond which noise began to be introduced in the data as observed in the 15cm point spacing cloud in figure 32.

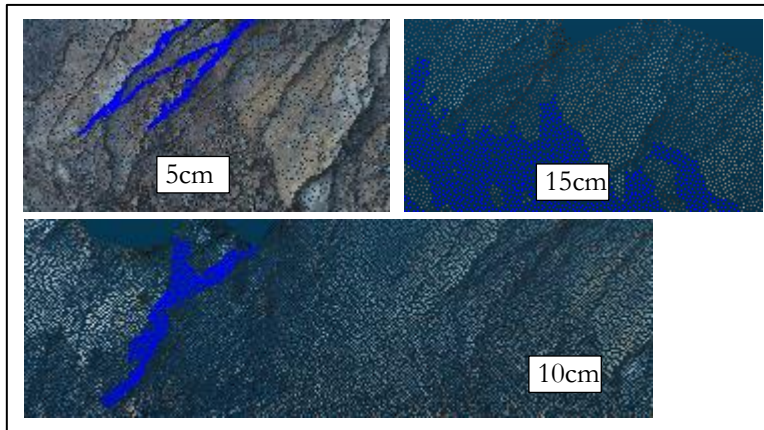


Figure 32: Overlap results between the resampled classified and RGB clouds at n_p 500 and other optimal parameters kept constant

from the use of the optimal values in the previous application suggesting that the knn parameter had the more influence on the extraction of the discontinuities from the point clouds than α and β . Further, n_p was increased from 50 to 500 and the other optimal parameters kept constant to check the responses of the resampled clouds. The results drastically changed as most of the small clusters of the planes were lost as shown in figure 32. The minimum point density required to effectively extract the discontinuities also changed from 43 pts/m² to 149 pts/m² which corresponded to the 10cm point spacing in the cloud beyond which noise began to be introduced in the data as observed in the 15cm point spacing cloud in figure 32. These results interestingly revealed that like knn, n_p also had a significant effect on recovery of the discontinuity sets from the point clouds and therefore, should be carefully optimized in order to obtain desirable results.

5. DISCUSSION AND CONCLUSIONS

The study aimed to investigate the effect of UAV flight plan and point cloud processing parameters on the characterization of the rock mass discontinuities. The drone data was acquired from the study area using automated and manual flights. Six UAV automated surveys were successfully conducted on slope 1 and a total of 616 images were captured. The average point densities of the raw point clouds generated from the six flights ranged from 321 points/m² or 2444 points/m³ to 682 points/m² or 5050 points/m³ as indicated in table 3 and appendix 2. On the other hand, 49 images were collected from slope 2 using a manual flight whose 3D model had an average point density of 2018 points/m² or 18080 points/m³. Alongside, the UAV survey, fourteen GCPs were collected using a differential GNSS receiver to enable precise georeferencing of some point clouds during image processing in order to compare the data quality with the other 3D models without GCPs.

The captured images were processed using pix4D and two sets of point clouds were generated, one set consisting of datasets with GCPs and the other set without GCPs. The results of precise georeferencing using GCPs reviewed that the models with GCPs improved the spatial accuracy evidenced by the displacement of the image block from the initial location (without GCPs) to its final position (with GCPs) as depicted by figure 10 in order to pin down the block to the correct geolocation on the ground. The model was displaced by 0.034m, 0.076m and 0.011m in the XYZ directions as observed in figure 11. This is because in the absence of GCPs, the resulting 3D model can easily stretch or warp due to the low accuracy of the UAV onboard GNSS and noise caused during photo stitching (Manconi et al., 2019; Menegoni et al., 2019; Nelms et al., 2018). The spatial accuracy differences in the two models leads to a conclusion that the model without GCPs cannot be relied on to provide accurate data required for the geomechanical characterization in order to provide correct advice to inform correct decision making regarding what type and where to implement rockfall mitigation measures.

The study area is a steep slope terrain, therefore, an appropriate approach of executing the UAV survey in the research area required careful flight planning in order to collect good quality data. For example, in studying the use of the drone to survey a coastal cliff face, Jaud et al. (2019) concluded that off nadir imaging angles of 20°, 30° and 40° aided in avoiding occlusions in the data due to the obstruction from the cliff. Further, Kozmus Trajkovski et al. (2020), Manconi et al. (2019) and Nesbit and Hugenholtz (2019) also submitted that the use of oblique images in digital photogrammetry significantly improved the spatial accuracy, precision and reduced the amount of missing data and systematic errors in the data. In this study, investigations to check the influence of the flight distance to the slope and the camera angle revealed markedly differences in the point density of the models obtained from the different perpendicular distances and tilt angles as shown in table 3. The model with the highest point density was obtained at the drone perpendicular distance of 36.3m to the slope with a camera tilt angle of 45° confirmed by its higher overall accuracy (47%) compared to the 33%-40% range of the other models as indicated in subsection 4.1.2.1. Therefore, the research concluded that flight distance and camera tilt angle had an influence on the quality of the UAV data, however, the camera tilt angle had more effect as it determined the perpendicular distance of the camera to the slope as illustrated in figure 5 and in table 3. Therefore, flight planning for similar UAV surveys for an area with similar average slope angle, geomechanical classification, platy limestone geological formation and fragmented discontinuity network should incorporate the flight distance of 36.3m and drone camera tilt angle of 45° in order to acquire data of the optimal point density for effective extraction and characterization of the discontinuities from such datasets. Additionally, visual assessment of the data showed differences in the scale of the observed discontinuities in the raw images obtained at different tilt angles.

This is an interesting observation that provides several options of visualizing the geological structures to better understand the geometrical properties of the discontinuities.

The study area is heavily vegetated as shown in figure 1. Unlike airborne LIDAR whose laser beam can penetrate between leaves, UAV optical cameras lack such capabilities resulting in occlusions and shadowing effect in the data especially below the canopy and behind the obstructed areas (Anders et al., 2019; Isenburg, 2014; Vosselman & Maas, 2010; Yilmaz et al., 2018). However, parametric processing requires a vegetation free 3D model for easy recognition of the geological structures and reduce inaccuracies in the results due to vegetation noise. Therefore, three automatic vegetation removal methods were explored to rid the datasets of vegetation. The traditional manual method, that involved segmenting out the vegetation via the segmentation tool in cloudcompare was used as a reference to the automated methods to check their effectiveness. The automated methods involved the use of software to remove vegetation from the messy point clouds. The algorithms investigated include CSF, a plugin in cloudcompare developed by Zhang et al. (2016), LAStools developed by Isenburg (2014) and CANUPO also a plugin in cloudcompare developed by Brodu and Lague (2012). By comparison, LAStools removed the most vegetation from the point clouds, its drawback however, was that it considerably removed part of the terrain points along with vegetation resulting in significant reduction in the point density of the data. The least performing algorithm was the CSF as shown by the large surface area covered by the residual vegetation on the cloud in relation to the total surface area of the cloud in figure 12. Overall, the canupo outperformed the other automatic methods as it removed a great deal of vegetation while retaining good amount of point density.

Following the successful pre-processing (manual vegetation removal) of the selected datasets, the candidate datasets were subjected to parametric processing to extract rock mass discontinuities in the point clouds. Qualitative analysis of the results showed that slope 2 data outperformed slope 1 data in the number of the discontinuities recovered from the point clouds. In slope 2 all the three main discontinuity sets verified using the orthophoto shown in figure 16 subsection 4.1.1.4 were successfully identified in all the experiments whereas in the slope 1 data not all the three sets were recovered in every experiment. J3 was particularly absent in most of the parameter test results.

Quantitatively, the overall accuracy computation results revealed that in the 2cm_GSD_45° model from slope 1, the highest overall accuracies for the knn, α and β were 40%, 40% and 47% respectively. This implied that on average, when the knn parameter was varied and the other parameters kept constant within the threshold values indicated in table 6 in subsection 4.1.1.1 the DSE could only effectively identify and extract 40% of all the thirty (30) sampled discontinuities from this data, another 40% if the α parameter was varied while knn, β and n_p were kept constant and 47% for the β if knn, α and n_p were kept fixed as described in subsection 4.1.2. These overall accuracies corresponded to the knn, α and β values of 10, 15° and 50° respectively. In the 2.5cm_GSD_45° model, the overall accuracies for the knn, α and β were 33%, 37% and 40% respectively. Similarly, DSE could only recognize and extract 33%, 37% and 40% of the total sampled discontinuities in this model when the tested parameters were varied and others kept constant as described earlier. The accuracy indices in the 2.5cm_GSD_45° model corresponded to the knn value of 30, α value of 15° and β value of 40°. The optimal parameter threshold values obtained were generally consistent with the findings of (Riquelme et al., 2014). However, as it be can inferred from the results of the overall accuracy computations, the results are not reliable because if the accuracies are below 50% then the operator is better off guessing empirically the parameter thresholds to predict the presence or absence of the discontinuities in a rock mass (Beguería, 2005; Lagomarsino et al., 2015).

The low overall accuracies in all the three experimented parameters in the slope 1 data which include 0% for the β value of 10° confirmed the reasons for the poor results described earlier as being attributed to the low quality of the data due to the presence of noise in the data. The presence of low vegetation, residual

vegetation from the vegetation removal process covering an area as high as 700m² of the total point cloud surface area (3400m²), shadowing effect from the higher vegetation, occlusions and lack of sufficient exposed rock mass surfaces on slope 1 contributed to the low quality of the data. The noise in the data hindered the algorithm to effectively identify and subsequently extract all the three discontinuity sets especially the sub vertical structures evidenced by the absence of J3 in some classified point clouds after the extraction process as shown in tables 8, 11, 12 and 13 in subsection 4.1.2.1 for example. In an effort to suppress the noise, n_p was increased from 50 to 500 leading to removal of the small joints (J3) during the clustering stage. The large n_p was necessitated in order to strike a balance between noise and accuracy at the expense of J3.

However, slope 2 data produced good overall accuracies as illustrated in figures 24, 25 and 26 in subsection 4.1.2.3. The computed accuracy indices for each of the tested parameter values showed that the highest overall accuracies for the three parameters keeping other parameters constant during individual parameter value test, were achieved at knn 40, α 15° and β 50° as shown in tables 14, 15 and 16 whose overall accuracies were 73%, 80% and 73% respectively. These accuracies entail that DSE effectively identified and extracted 73%, 80% and 73% of all the sampled discontinuity sets at the optimal knn , α and β values respectively. The good results were attributed to the good quality data of slope 2 due to the absence of occlusions, less shadowing effect in the data, less undulations on the slope surface and more exposure of the rock mass surface, good view angle of the camera and short UAV perpendicular distance to the slope.

Spatial resolution sensitivity analysis results generally revealed that knn and n_p had the most influence on the minimum point density requirements for the discontinuity set extraction as illustrated in figures 31 and 32. This is particularly important because the optimal recovery of the discontinuity sets from the point clouds in a similar research work will largely depend on these parameters. Further, the differences in the overall accuracies between the 2cm_GSD_45° and 2.5cm_GSD_45° models confirmed that point density affects the extraction of the rock mass discontinuities in a point cloud.

Qualitative analysis on the influence of varying the parameter values on the automatic extraction of the discontinuities in a rock mass by DSE reviewed that reducing knn favours the extraction of more horizontal discontinuities while increasing the three parameters within the tested ranges favoured the extraction of more sub vertical structures from the point clouds than horizontal structures. This observation is important because it provided a clue at a glance of how the parameters should be optimized in order to obtain the optimal results depending on the objectives of the research. For example, if the interest is the horizontal discontinuities because they largely affect slope stability, then the knn value should be set to the minimum threshold or as close to the minimum as practically possible while keeping α , β and n_p constant so as to maximize the extraction of the horizontal structures to facilitate further analysis and properly inform the implementation of appropriate mitigations against rockfalls.

The analysis of the joint sets dip/dip directions of the recovered geological structures showed a consistent trend in dip and dip direction as shown in figures 27 and 28 between the automatic and manually obtained observations. It was also observed that J2 and J3 have larger dip angles compared to J1 an indication that J2 and J3 are sub vertical structures whereas J1 is horizontal and dip in the same direction (parallel) as the slope. The trend was similar in slope 2 data. Extra checks reviewed that there was a slight shift in the orientation of J3 between the two models in the two stereographic projection results. The geometric properties of the extracted discontinuities are predominantly of tiny spacing of in the order of 10cm and non-persistent in the order of 0m confirmed from the measurements on the point cloud via the point picking tool in cloudcompare and from the scanline measurements obtained in the field as shown in appendix 4 creating a

fragmented discontinuity network evidenced by the small blocks of detached rocks and scree deposits along the trajectory of the rock falls in the study area observed during the field visit.

With respect to the objective of the study, the following conclusions were drawn:

Undertaking a similar research in a similar study area, using an automated UAV survey, should incorporate the perpendicular distance to slope of 36.3m or closer to the slope and camera tilt angle of 45° into the flight plan. Georeferencing significantly improved the spatial accuracy of the 3D model by pinning it to its correct geolocation on the ground in all the three XYZ direction. The UAV camera oblique angle had more influence on the point density of the drone data than the perpendicular distance of the drone to the slope. This was attributed to fact that the oblique angle of the UAV camera determined the its perpendicular distance to the slope. Further, the different camera oblique angles impacted differently on point densities of the data to the worst being extreme slanting angle (30°). Therefore, UAV camera tilt angle should carefully be planned during flight planning to ensure that the look angle of the drone is as perpendicular to the slope as practically possible depending on the slope angle. The optimal parameter values in DSE to ensure successful extraction and characterization of the discontinuity sets in a rock mass of a study area with slope angle, slope rating mass, platy limestone geology and fragmented discontinuity network similar to the study area are: k_{nn} 40, α 15° , β 50° and n_p 50. Also, point density of the UAV photogrammetry data depicting terrains like the study area, affects the extraction of the rock mass discontinuities from such datasets. There are three major discontinuity sets in the study area. Two of the three namely J2 and J3 are sub vertical with similar geometrical characteristics while J1 is horizontal orienting in the same direction as the slope surface at slope 1. Similarly, on slope 2, the horizontal structures are the bedding planes whereas the sub vertical joints are J1 and J2.

Further research is recommended in the following:

Future research is recommended to quantitatively investigate the influence of roughness on the extraction of the discontinuities from a rock mass with high roughness. The research faced serious challenges to automatically remove vegetation from the collected data since most of the algorithms were still undergoing refinement at the time of the study. Others, like LAsTools though effective, are largely meant for the LIDAR data and not UAV. Therefore, future research is highly recommended to fully investigate the vegetation removal capabilities of the canupo plugin in cloudcompare as it outperformed the other automated methods and therefore, has a potential of being a very useful tool in such a research work. Lastly, future studies can consider checking the influence of other parameters not tested in this research in other terrains with different characteristics and check how the requirements of flight planning and discontinuity set extraction would change or compare with the results obtained in this research.

LIST OF REFERENCES

- Admassu, Y., & Shakoor, A. (2012). DIPANALYST: A computer program for quantitative kinematic analysis of rock slope failures. *Computers and Geosciences*, *54*, 196–202. <https://doi.org/10.1016/j.cageo.2012.11.018>
- Agliardi, F., Crosta, G. B., Meloni, F., Valle, C., & Rivolta, C. (2013). Structurally-controlled instability, damage and slope failure in a porphyry rock mass. *Tectonophysics*, *605*, 34–47. <https://doi.org/10.1016/j.tecto.2013.05.033>
- Anders, N., Valente, J., Masselink, R., & Keesstra, S. (2019). Comparing Filtering Techniques for Removing Vegetation from UAV-Based Photogrammetric Point Clouds. *Drones*, *3*, 61. <https://doi.org/10.3390/drones3030061>
- Bad Elf. (2020). *Post-processing GNSS Data with RTKLIB - Introduction - Bad Elf*. Retrieved from: <https://bad-elf.com/pages/post-processing-gnss-data-with-rtklib-introduction>
- Banko, G. (1998). A review of assessing the accuracy of and of methods including remote sensing data in forest inventory. *Internation Institute for Applied Systems Analysis, Interim Report IT-98-081, November, Laxenburg, Austria*.
- Beguería, S. (2005). Validation and evaluation of predictive models in hazard assessment and risk management. *Natural Hazards*, *37*, 315–329. <https://doi.org/10.1007/s11069-005-5182-6>
- Brodu, N., & Lague, D. (2012). 3D terrestrial lidar data classification of complex natural scenes using a multi-scale dimensionality criterion: Applications in geomorphology. *ISPRS Journal of Photogrammetry and Remote Sensing*, *68*(1), 121–134. <https://doi.org/10.1016/j.isprsjprs.2012.01.006>
- Bühler, Y., Christen, M., Glover, J., Christen, M., & Bartelt, P. (2016). Significance of digital elevation model resolution for numerical rockfall simulation. *3rd International Symposium Rock Slope Stability, November*, 101–102. <https://www.researchgate.net/publication/311021182>
- Crosta, G. B., & Agliardi, F. (2003). A methodology for physically based rockfall hazard assessment. *Natural Hazards and Earth System Science*, *3*, 407–422. <https://doi.org/10.5194/hal-00301598>
- Dewez, T. J. B., Girardeau-Montaut, D., Allanic, C., & Rohmer, J. (2016). Facets : A cloudcompare plugin to extract geological planes from unstructured 3d point clouds. *International Archives of the Photogrammetry, Remote Sensing and Spatial Information Sciences - ISPRS Archives, XLI-B5, 20*, 799–804. <https://doi.org/10.5194/isprsarchives-XLI-B5-799-2016>
- ELtohamy, F., & Hamza, E. H. (2009). Effect of Ground Control points Location and Distribution on Geometric Correction Accuracy of Remote Sensing Satellite Images. *13th International Conference on AEROSPACE SCIENCES & AVIATION TECHNOLOGY, ASAT- 13, May 26 – 28*, 1–14. <http://www.mtc.edu.eg/ASAT13/pdf/RS06.pdf>
- Ester, M., Kriegel, H.-P., Sander, J., & Xu, X. (1996). Density-Based Clustering Methods. *Comprehensive Chemometrics*. www.aaii.org
- Fadakar Alghalandis, Y. (2017). ADFNE: Open source software for discrete fracture network engineering, two and three dimensional applications. *Computers and Geosciences*, *102*, 1–11. <https://doi.org/10.1016/j.cageo.2017.02.002>
- Fadakar Alghalandis, Y., Elmo, D., & Eberhardt, E. (2017). *Similarity Analysis of Discrete Fracture Networks. January 2018*, 0–20. Retrieved from: <https://www.semanticscholar.org/paper/Similarity-Analysis-of-Discrete-Fracture-Networks-Alghalandis-Elmo/4716563c3f54fae44091f573814dde36550ac7f8>
- Fanos, A. M., & Pradhan, B. (2018a). A novel rockfall hazard assessment using laser scanning data and 3D modelling in GIS. *Catena*, *172*, 435–450. <https://doi.org/10.1016/j.catena.2018.09.012>
- Fanos, A. M., & Pradhan, B. (2018b). Laser Scanning Systems and Techniques in Rockfall Source Identification and Risk Assessment: A Critical Review. *Earth Systems and Environment*, *2*, 163–182. <https://doi.org/10.1007/s41748-018-0046-x>
- Gerke, M., & Przybilla, H. J. (2016). Accuracy analysis of photogrammetric UAV image blocks: Influence of onboard RTK-GNSS and cross flight patterns. *Photogrammetry, Fernerkundung, Geoinformation*, *2016*(1), 17–30. <https://doi.org/10.1127/pfg/2016/0284>
- Girardeau-Montaut, D. (2015). CloudCompare: 3D point cloud and mesh processing software. Retrieved from: <http://www.cloudcompare.org>.
- Gnyawali, K. R., Shrestha, R., Bhattarai, A., Magar, P. R., Dhungana, A. R., Sukupayo, I., & Dumaru, R.

- (2016). Rockfall Characterization and Structural Protection in the Siddhababa Section of Siddhartha Highway H10, Nepal. *Journal of the Institute of Engineering*, 11(1), 1–11.
<https://doi.org/https://doi.org/10.3126/jie.v11i1.14689>
- Gomez, C., & Purdie, H. (2016). UAV- based Photogrammetry and Geocomputing for Hazards and Disaster Risk Monitoring – A Review. *Geoenvironmental Disasters*, 3(1).
<https://doi.org/10.1186/s40677-016-0060-y>
- Guzzetti, F., Crosta, G., Detti, R., & Agliardi, F. (2002). STONE: A computer program for the three-dimensional simulation of rock-falls. *Computers and Geosciences*, 28(2002), 1079–1093.
[https://doi.org/10.1016/S0098-3004\(02\)00025-0](https://doi.org/10.1016/S0098-3004(02)00025-0)
- Hack, R. (1998). SLOPE STABILITY PROBABILITY CLASSIFICATION 2nd edition. In 43. International Institute for Aerospace Survey and Earth Sciences (ITC).
- Hackney, C., & Clayton, A. I. (2015). Unmanned Aerial Vehicles (UAVs) and their application in geomorphic mapping. *Geomorphological Techniques*, 7, 1–12.
<http://eprints.soton.ac.uk/id/eprint/376639>
- Haneberg, W. C. (2008). Using close range terrestrial digital photogrammetry for 3-D rock slope modeling and discontinuity mapping in the United States. *Bulletin of Engineering Geology and the Environment*, 67(4), 457–469. <https://doi.org/10.1007/s10064-008-0157-y>
- Hoek, E. (2006). *Practical Rock Engineering - Notes*. Evert Hoek Consulting Engineer Inc.
- Hugenholtz, C. H., Whitehead, K., Brown, O. W., Barchyn, T. E., Moorman, B. J., LeClair, A., Riddell, K., & Hamilton, T. (2013). Geomorphological mapping with a small unmanned aircraft system (sUAS): Feature detection and accuracy assessment of a photogrammetrically-derived digital terrain model. *Geomorphology*, 194, 16–24. <https://doi.org/10.1016/j.geomorph.2013.03.023>
- Isenburg, M. (2014). *Efficient LIDAR processing software (version 141017 academic)*. Reterived from:
<https://rapidlasso.com/LAStools/>
- Jaboyedoff, M., Dudt, J. P., & Labiouse, V. (2005). An attempt to refine rockfall hazard zoning based on the kinetic energy, frequency and fragmentation degree. *Natural Hazards and Earth System Science*, 5, 621–632. <https://www.nat-hazards-earth-syst-sci.net/5/621/2005/>
- Jaud, M., Letortu, P., Théry, C., Grandjean, P., Costa, S., Maquaire, O., Davidson, R., & Le Dantec, N. (2019). UAV survey of a coastal cliff face – Selection of the best imaging angle. *Measurement: Journal of the International Measurement Confederation*, 139, 10–20.
<https://doi.org/10.1016/j.measurement.2019.02.024>
- Kozmus Trajkovski, K., Grigillo, D., & Petrovič, D. (2020). Optimization of UAV Flight Missions in Steep Terrain. *Remote Sensing*, 12(8), 1293. <https://doi.org/10.3390/rs12081293>
- Lagomarsino, D., Segoni, S., Rosi, A., Rossi, G., Battistini, A., Catani, F., & Casagli, N. (2015). Quantitative comparison between two different methodologies to define rainfall thresholds for landslide forecasting. *Natural Hazards and Earth System Sciences*, 15(10), 2413–2423.
<https://doi.org/10.5194/nhess-15-2413-2015>
- Lato, M. J., Diederichs, M. S., & Hutchinson, D. J. (2010). Bias correction for view-limited lidar scanning of rock outcrops for structural characterization. *Rock Mechanics and Rock Engineering*, 43(5), 615–625.
<https://doi.org/10.1007/s00603-010-0086-5>
- Lee, J., & Sung, S. (2016). Evaluating spatial resolution for quality assurance of UAV images. *Spatial Information Research*, 24(2), 141–154. <https://doi.org/10.1007/s41324-016-0015-0>
- Lei, Q., Latham, J. P., & Tsang, C. F. (2017). The use of discrete fracture networks for modelling coupled geomechanical and hydrological behaviour of fractured rocks. *Computers and Geotechnics*, 85, 151–176.
<https://doi.org/10.1016/j.compgeo.2016.12.024>
- Manconi, A., Ziegler, M., Blöchliger, T., & Wolter, A. (2019). Technical note: optimization of unmanned aerial vehicles flight planning in steep terrains. In *International Journal of Remote Sensing* (Vol. 40, Issue 7, pp. 2483–2492). Taylor & Francis. <https://doi.org/10.1080/01431161.2019.1573334>
- Matej, Z., Amiri, M., Cvachovec, F., Prenosil, V., Mravec, F., & Kopecky, Z. (2014). Digital two-parametric processing of the output data from radiation detectors. *Progress in Nuclear Science and Technology*, 4, 670–674. <https://doi.org/10.15669/pnst.4.670>
- Menegoni, N., Giordan, D., Perotti, C., & Tannant, D. D. (2019). Detection and geometric characterization of rock mass discontinuities using a 3D high-resolution digital outcrop model generated from RPAS imagery – Ormea rock slope, Italy. *Engineering Geology*, 252(March 2018), 145–163. <https://doi.org/10.1016/j.enggeo.2019.02.028>


- Nagendran, S. K., Ismail, M. A. M., & Tung, W. Y. (2019). Integration of UAV photogrammetry and kinematic analysis for rock slope stability assessment. *Bulletin of the Geological Society of Malaysia*, 67, 105–111. <https://www.researchgate.net/publication/334061941>
- Nelms, R. J., Hovorka, A. M., Spencer, K. W., Mcmillan, R. M., Fry, C., James, R., & Smith, W. D. (2018). *How Best to Use Ground Control in Drone Surveying*. Retrieved from: www.californiasurveyors.com
- Nesbit, P. R., & Hugenholtz, C. H. (2019). Enhancing UAV-SfM 3D model accuracy in high-relief landscapes by incorporating oblique images. *Remote Sensing*, 11(3), 1–24. <https://doi.org/10.3390/rs11030239>
- Oniga, E., Breaban, A., & Statescu, F. (2018). Determining the optimum number of ground control points for obtaining high precision results based on UAS images. *Mdpi*, 2, 352. <https://doi.org/10.3390/eecs-2-05165>
- Pellicani, R., Spilotro, G., & Van Westen, C. J. (2016). Rockfall trajectory modeling combined with heuristic analysis for assessing the rockfall hazard along the Maratea SS18 coastal road (Basilicata, Southern Italy). *Landslides*, 13(5), 985–1003. <https://doi.org/10.1007/s10346-015-0665-3>
- Pepe, M., Fregonese, L., & Scaioni, M. (2018). Planning airborne photogrammetry and remote-sensing missions with modern platforms and sensors. *European Journal of Remote Sensing*, 51(1), 412–435. <https://doi.org/10.1080/22797254.2018.1444945>
- pix4D. (2011). *Processing options*. Retrieved from: <https://support.pix4d.com/hc/en-us/articles/202557799>
- Pradhan, B., & Sameen, M. I. (2017). Laser scanning systems in landslide studies. In *Laser Scanning Applications in Landslide Assessment*. https://doi.org/10.1007/978-3-319-55342-9_1
- Rahl, J. M., Fassoulas, C., & Brandon, M. T. (2004). *EXHUMATION OF HIGH-PRESSURE METAMORPHIC ROCKS WITHIN AN ACTIVE CONVERGENT MARGIN, CRETE, GREECE*. Retrieved from: <http://www.isprambiente.gov.it/files/pubblicazioni/periodicitecnici/memorie/memorie/xiii/b32.pdf>
- Region of Crete. (2017). *Building Regional Actions for New Developments in Tourism*.
- Remondino, F., Barazzetti, L., Nex, F., Scaioni, M., & Sarazzi, D. (2012). Uav Photogrammetry for Mapping and 3D Modeling – Current Status and Future Perspectives. *ISPRS - International Archives of the Photogrammetry, Remote Sensing and Spatial Information Sciences*, XXXVIII-1/(September), 25–31. <https://doi.org/10.5194/isprsarchives-xxxviii-1-c22-25-2011>
- Remondino, Fabio, Nocerino, E., Toschi, I., & Menna, F. (2017). A critical review of automated photogrammetric processing of large datasets. *International Archives of the Photogrammetry, Remote Sensing and Spatial Information Sciences - ISPRS Archives*, 42(2W5), 591–599. <https://doi.org/10.5194/isprs-archives-XLII-2-W5-591-2017>
- Riquelme, A., Abellán, A., Tomás, R., & Jaboyedoff, M. (2014). A new approach for semi-automatic rock mass joints recognition from 3D point clouds. *Computers and Geosciences*, 68, 38–52. <https://doi.org/10.1016/j.cageo.2014.03.014>
- Romana, M., Serón, J. B., & Montalar, E. (2003). SMR geomechanics classification: Application, experience and validation. *10th ISRM Congress*, 4(iii), 981–984.
- RTKLIB. (2011). *RTKLIB ver. 2.4.1 Manual* (Vol. 80, Issue 6, pp. 064711–064711).
- Salvini, R., Mastroiocco, G., Seddaiu, M., Rossi, D., & Vanneschi, C. (2017). The use of an unmanned aerial vehicle for fracture mapping within a marble quarry (Carrara, Italy): photogrammetry and discrete fracture network modelling. *Geomatics, Natural Hazards and Risk*, 8(1), 34–52. <https://doi.org/10.1080/19475705.2016.1199053>
- Sanz-Ablanedo, E., Chandler, J. H., Rodríguez-Pérez, J. R., & Ordóñez, C. (2018). Accuracy of Unmanned Aerial Vehicle (UAV) and SfM photogrammetry survey as a function of the number and location of ground control points used. *Remote Sensing - MDPI*, 10(10). <https://doi.org/10.3390/rs10101606>
- Saroglou, C. (2019). GIS-based rockfall susceptibility zoning in Greece. *Geosciences (Switzerland)*, 9(4). <https://doi.org/10.3390/geosciences9040163>
- Sedorovich, A., Hara, C. O., & Schuckman, K. (2010). Image Accuracy Checkpoint Collection Guide. *PositionIT*, 46–49. [http://www.ee.co.za/wp-content/uploads/legacy/PositionIT 2009/PositionIT 2010/image accuracy.pdf](http://www.ee.co.za/wp-content/uploads/legacy/PositionIT%202009/PositionIT%202010/image%20accuracy.pdf)
- Slob, S., Hack, H. R. G. K., Feng, Q., Röshoff, K., & Turner, A. K. (2007). Fracture mapping using 3D laser scanning techniques. *11th Congress of the International Society for Rock Mechanics, July*, 299–302.
- Slob, Siefko. (2010). *Automated rock mass characterisation using 3-D terrestrial laser scanning*. Wöhrmann Print

- Service. <http://www.narcis.nl/publication/RecordID/oai:tudelft.nl:uuid:c1481b1d-9b33-42e4-885a-53a6677843f6>
- SPH-Engineering. (2019). *User Manual* © 2019 (Vol. 3, Issue 438, pp. 1–82).
- Spreadico, M. C., Franci, F., Bitelli, G., Borgatti, L., & Ghirotti, M. (2017). Intact rock bridge breakage and rock mass fragmentation upon failure: quantification using remote sensing techniques. *Photogrammetric Record*, 32(160), 513–536. <https://doi.org/10.1111/phor.12225>
- Story, M., & Congalton, R. G. (1986). Remote Sensing Brief Accuracy Assessment: A User's Perspective. *Photogrammetric Engineering and Remote Sensing*, 52(3), 397–399.
- Tannant, D. (2015). Review of Photogrammetry-Based Techniques for Characterization and Hazard Assessment of Rock Faces. *International Journal of Geohazards and Environment*, 1, 76–87. <https://doi.org/10.15273/ijge.2015.02.009>
- UNDRR. (2019). *Disaster Data and Statistics*. Retrieved from: <https://www.preventionweb.net/knowledgebase/disaster-statistics>
- Vosselman, G., & Maas, H. (Eds.). (2010). *Airborne and terrestrial laser scanning*. Whittles Publishing. <https://doi.org/10.1080/17538947.2011.553487>
- Wang, X., Zou, L., Shen, X., Ren, Y., & Qin, Y. (2017). A region-growing approach for automatic outcrop fracture extraction from a three-dimensional point cloud. *Computers and Geosciences*, 99(September 2016), 100–106. <https://doi.org/10.1016/j.cageo.2016.11.002>
- Wei, Y. M., Kang, L., Yang, B., & Wu, L. Da. (2013). Applications of structure from motion: A survey. *Journal of Zhejiang University: Science C*, 14(7), 486–494. <https://doi.org/10.1631/jzus.CIDE1302>
- west-crete.com. (1999). *Geology and formation of the Samaria gorge*. <https://www.west-crete.com/samaria-gorge-geology.htm>
- wordpress.com. (n.d.). *Geology | Samaria National Park - ΣΑΜΑΡΙΑ ΕΘΝΙΚΟΣ ΔΡΥΜΟΣ*. Retrieved May 20, 2020, from <https://samarianationalpark.wordpress.com/geology/>
- Wyllie, D., & Mah, C. (2005). *Rock Slope Engineering: Civil and Mining* (E. Hoek & J. Bray (Eds.); 4th Edition). Taylor & Francis.
- Yilmaz, V., Konakoglu, B., Serifoglu, C., Gungor, O., & Gokalp, E. (2018). Image classification-based ground filtering of point clouds extracted from UAV-based aerial photos. *Geocarto International*, 33(3), 310–320. <https://doi.org/10.1080/10106049.2016.1250825>
- Žabota, B., Repe, B., & Kobal, M. (2019). Influence of digital elevation model resolution on rockfall modelling. *Geomorphology*, 328, 183–195. <https://doi.org/10.1016/j.geomorph.2018.12.029>
- Zhang, W., Qi, J., Wan, P., Wang, H., Xie, D., Wang, X., & Yan, G. (2016). An easy-to-use airborne LiDAR data filtering method based on cloth simulation. *Remote Sensing*, 8(6). <https://doi.org/10.3390/rs8060501>
- Zieher, T., Formanek, T., Bremer, M., Meissl, G., & Rutzinger, M. (2012). Digital Terrain Model Resolution and its Influence on Estimating the Extent of Rockfall Areas. *Transactions in GIS*, 16(5), 691–699. <https://doi.org/10.1111/j.1467-9671.2012.01334.x>


APPENDICES



Appendix 1: An extract of the summary of the quality report


Quality Report



Generated with Pix4Dmapper version 4.4.12

 **Important:** Click on the different icons for:











-  Help to analyze the results in the Quality Report
-  Additional information about the sections

 Click [here](#) for additional tips to analyze the Quality Report

Summary

Project	2cm_GSD_60_GCP
Processed	2020-03-04 03:30:16
Camera Model Name(s)	FC330_3.6_4000x3000 (RGB)
Average Ground Sampling Distance (GSD)	2.05 cm / 0.81 in
Area Covered	0.108 km ² / 10.7591 ha / 0.04 sq. mi. / 26.6001 acres
Time for Initial Processing (without report)	06m:38s

Quality Check

 Images	median of 56645 keypoints per image	
 Dataset	97 out of 97 images calibrated (100%), all images enabled	
 Camera Optimization	2.29% relative difference between initial and optimized internal camera parameters	
 Matching	median of 21367.6 matches per calibrated image	
 Georeferencing	yes, 2 GCPs (2 3D), mean RMS error = 0.001 m	

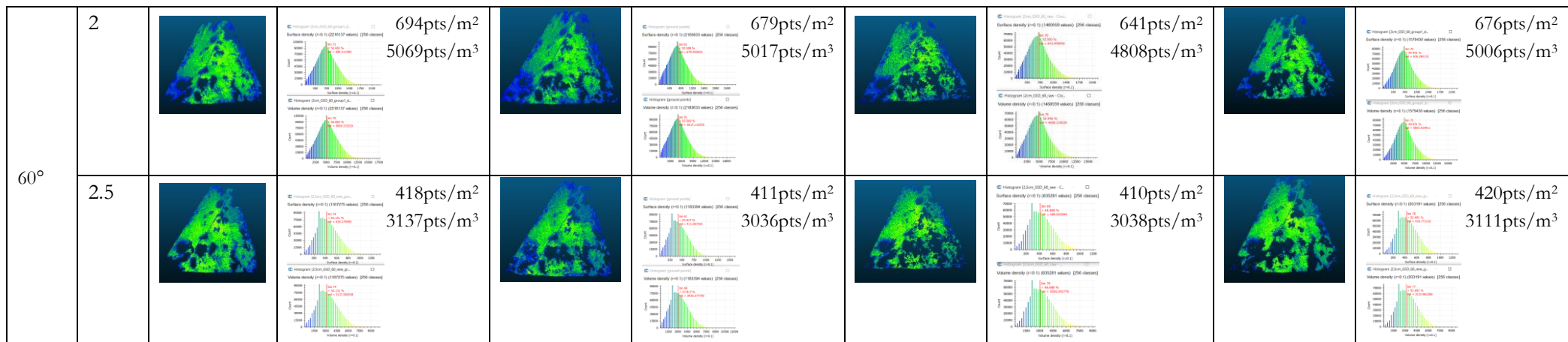
Appendix 2a: Results of the point cloud quality with GCPs

Tilt angle	GSD (cm)	Point cloud quality with GCPs							
		Manual	Point density @ 50% of total number of points	CSF	Point density @ 50% of total number of points	LAStools	Point density @ 50% of total number of points	CANUPO	Point density @ 50% of total number of points
30°	2		 631pts/m ² 4732pts/m ³		 622pts/m ² 4603pts/m ³		 573pts/m ² 4297pts/m ³		 622pts/m ² 4603pts/m ³
	2.5		 321pts/m ² 2444pts/m ³		 324pts/m ² 2432pts/m ³		 321pts/m ² 2365pts/m ³		 322pts/m ² 2413pts/m ³
45°	2		 682pts/m ² 5050pts/m ³		 648pts/m ² 4800pts/m ³		 631pts/m ² 4609pts/m ³		 658pts/m ² 4872pts/m ³
	2.5		 382pts/m ² 2863pts/m ³		 371pts/m ² 2783pts/m ³		 353pts/m ² 2686pts/m ³		 378pts/m ² 2839pts/m ³
60°	2		 622pts/m ² 4603pts/m ³		 615pts/m ² 4551pts/m ³		 580pts/m ² 4351pts/m ³		 604pts/m ² 4530pts/m ³

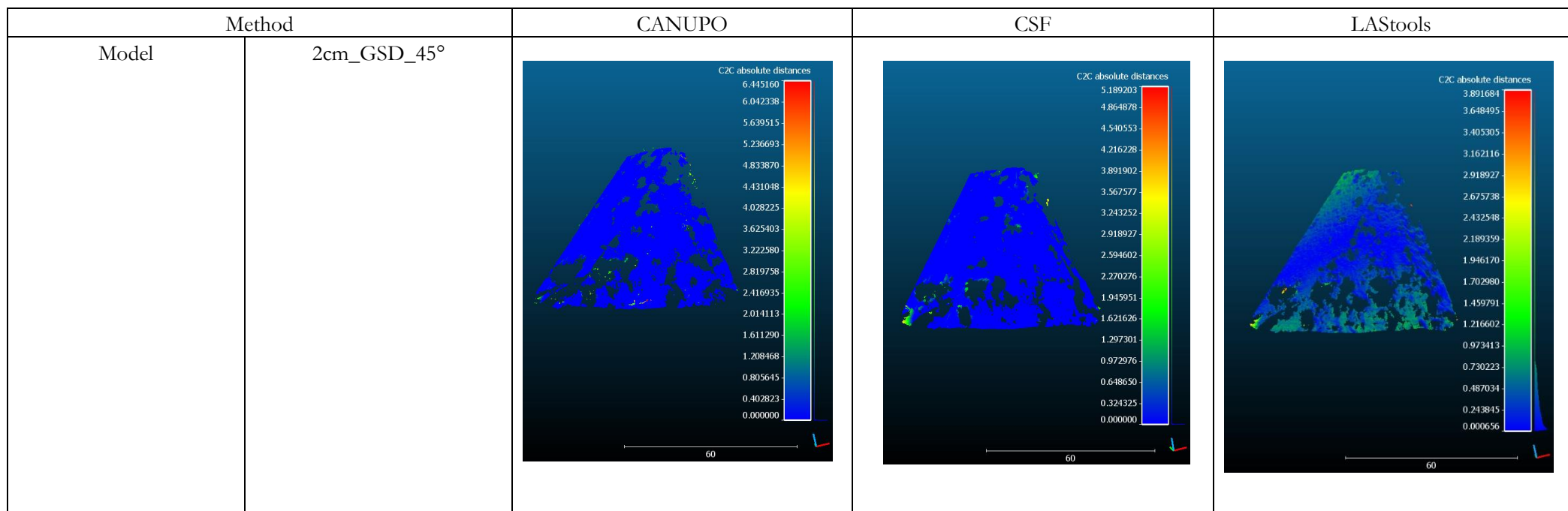
	2.5		 381pts/m ² 2857pts/m ³		 360pts/m ² 2742pts/m ³		 353pts/m ² 2684pts/m ³		 354pts/m ² /m ³
--	-----	--	---	--	---	--	---	--	--

Appendix 2b: Results of the point cloud quality without GCPs.

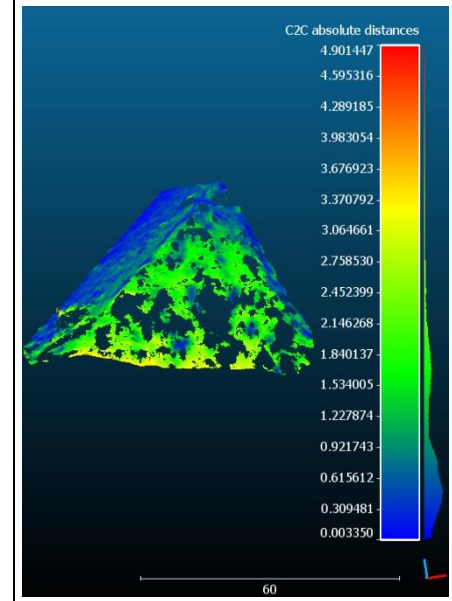
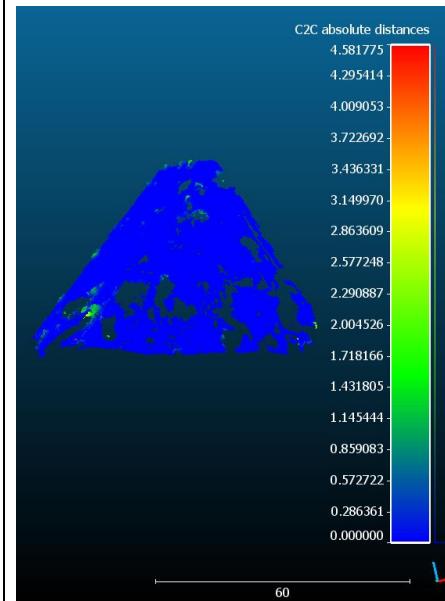
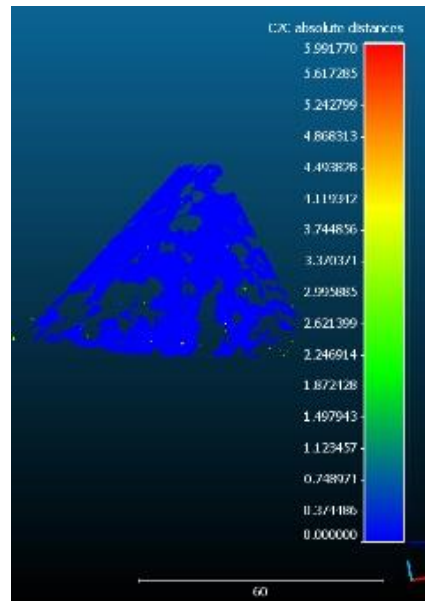
Tilt angle	GSD (cm)	Point cloud quality without GCPs							
		Reference (Manual)	Point density @ 50% of total number of points	CSF	Point density @ 50% of total number of points	LAStools	Point density @ 50% of total number of points	CANUPO	Point density @ 50% of total number of points
30°	2		 704pts/m ² 5344pts/m ³		 673pts/m ² 5050pts/m ³		 667pts/m ² 5004pts/m ³		 668pts/m ² 5088pts/m ³
	2.5		 323pts/m ² 2463pts/m ³		 323pts/m ² 2463pts/m ³		 322pts/m ² 2418pts/m ³		 330pts/m ² 2432pts/m ³
45°	2		 777pts/m ² 5759pts/m ³		 750pts/m ² 5554pts/m ³		 703pts/m ² 5271pts/m ³		 722pts/m ² 5342pts/m ³
	2.5		 392pts/m ² 2941pts/m ³		 382pts/m ² 2906pts/m ³		 380pts/m ² 2850pts/m ³		 385pts/m ² 2887pts/m ³



Appendix 2c: Results of the C2C distance computation



2.5cm_GSD_45°



Appendix 3a: Classification accuracy indices for 2cm_GSD_45° model on slope 1

knn₅

		Actual				Accuracy indices (%)				
		J1	J2	J3	NO	Total	CE	OE	UA	PA
Predicted	J1	9	7	4	0	20	55	10	45	90
	J2	0	0	0	0	0	0	100	0	0
	J3	0	0	0	0	0	0	100	0	0
	NO	1	3	6	0	10	100	0	0	0
	Total	10	10	10	0	30	Overall Accuracy (%)			30

knn₁₀

		Actual				Accuracy indices (%)				
		J1	J2	J3	NO	Total	CE	OE	UA	PA
Predicted	J1	9	7	6	0	22	59.09091	10	40.90909	90
	J2	1	3	2	0	6	50	70	50	30
	J3	0	0	0	0	0	0	100	0	0
	NO	0	0	2	0	2	100	0	0	0
	Total	10	10	10	0	30	Overall Accuracy (%)			40

knn₂₀

		Actual				Accuracy indices (%)				
		J1	J2	J3	NO	Total	CE	OE	UA	PA
Predicted	J1	8	7	4	0	19	57.89474	20	42.10526	80
	J2	2	2	3	0	7	71.42857	80	28.57143	20
	J3	0	0	0	0	0	0	100	0	0
	NO	0	1	3	0	4	100	0	0	0
	Total	10	10	10	0	30	Overall Accuracy (%)			33.33

knn₃₀

		Actual				Accuracy indices (%)				
		J1	J2	J3	NO	Total	CE	OE	UA	PA
Predicted	J1	7	6	4	0	17	58.82353	30	41.17647	70
	J2	2	2	1	0	5	60	80	40	20
	J3	1	1	0	0	2	100	100	0	0
	NO	0	1	5	0	6	100	0	0	0
	Total	10	10	10	0	30	Overall Accuracy (%)			30

knn₄₀

		Actual				Accuracy indices (%)				
		J1	J2	J3	NO	Total	CE	OE	UA	PA
Predicted	J1	6	6	4	0	16	62.5	40	37.5	60
	J2	2	2	1	0	5	60	80	40	20
	J3	1	1	1	0	3	66.66667	90	0	10
	NO	1	1	4	0	6	100	0	0	0
	Total	10	10	10	0	30	Overall Accuracy (%)			30

knn₅₀

		Actual				Accuracy indices (%)				
		J1	J2	J3	NO	Total	CE	OE	UA	PA
Predicted	J1	8	7	5	0	20	60	20	40	80
	J2	2	3	2	0	7	57.14286	70	42.85714	30
	J3	0	0	0	0	0	0	100	0	0
	NO	0	0	3	0	3	100	0	0	0
	Total	10	10	10	0	30	Overall Accuracy (%)			36.67

knn₆₀

		Actual				Accuracy indices (%)				
		J1	J2	J3	NO	Total	CE	OE	UA	PA
Predicted	J1	7	7	5	0	19	63.15789	30	36.84211	70
	J2	2	1	2	0	5	80	90	20	10
	J3	1	1	0	0	2	100	100	0	0
	NO	0	1	3	0	4	100	0	0	0
	Total	10	10	10	0	30	Overall Accuracy (%)			26.67

 α_5

		Actual				Accuracy indices (%)				
		J1	J2	J3	NO	Total	CE	OE	UA	PA
Predicted	J1	7	7	5	0	19	63.15789	30	36.84211	70
	J2	1	0	0	0	1	100	100	0	0
	J3	1	1	0	0	2	100	100	0	0
	NO	1	2	5	0	8	100	0	0	0
	Total	10	10	10	0	30	Overall Accuracy (%)			23.33

 α_{10}

		Actual				Accuracy indices (%)				
		J1	J2	J3	NO	Total	CE	OE	UA	PA
Predicted	J1	7	7	6	0	20	65	30	35	70
	J2	2	2	1	0	5	60	80	40	20
	J3	1	1	0	0	2	100	100	0	0
	NO	0	0	3	0	3	100	0	0	0
	Total	10	10	10	0	30	Overall Accuracy (%)			30

α_{15}

		Actual				Accuracy indices (%)				
		J1	J2	J3	NO	Total	CE	OE	UA	PA
Predicted	J1	8	7	5	0	20	60	20	40	80
	J2	2	3	2	0	7	57.14286	70	42.85714	30
	J3	0	0	1	0	1	0	90	0	10
	NO	0	0	2	0	2	100	0	0	0
	Total	10	10	10	0	30	Overall Accuracy (%)			40

 α_{20}

		Actual				Accuracy indices (%)				
		J1	J2	J3	NO	Total	CE	OE	UA	PA
Predicted	J1	8	7	6	0	21	61.90476	20	38.09524	80
	J2	2	3	3	0	8	62.5	70	37.5	30
	J3	0	0	0	0	0	0	100	0	0
	NO	0	0	1	0	1	100	0	0	0
	Total	10	10	10	0	30	Overall Accuracy (%)			36.67

 α_{30}

		Actual				Accuracy indices (%)				
		J1	J2	J3	NO	Total	CE	OE	UA	PA
Predicted	J1	8	6	6	0	20	60	20	40	80
	J2	2	3	3	0	8	62.5	70	37.5	30
	J3	0	0	0	0	0	0	100	0	0
	NO	0	1	1	0	2	100	0	0	0
	Total	10	10	10	0	30	Overall Accuracy (%)			36.67

 α_{40}

		Actual				Accuracy indices (%)				
		J1	J2	J3	NO	Total	CE	OE	UA	PA
Predicted	J1	0	0	0	0	0	0	100	0	0
	J2	2	3	3	0	8	62.5	70	37.5	30
	J3	0	0	0	0	0	0	100	0	0
	NO	8	7	7	0	22	100	0	0	0
	Total	10	10	10	0	30	Overall Accuracy (%)			10

 α_{50}

		Actual				Accuracy indices (%)				
		J1	J2	J3	NO	Total	CE	OE	UA	PA
Predicted	J1	0	0	0	0	0	0	100	0	0
	J2	2	3	3	0	8	62.5	70	37.5	30
	J3	0	0	0	0	0	0	100	0	0
	NO	8	7	7	0	22	100	0	0	0
	Total	10	10	10	0	30	Overall Accuracy (%)			10

β_{10}

		Actual				Accuracy indices (%)				
		J1	J2	J3	NO	Total	CE	OE	UA	PA
Predicted	J1	0	0	0	0	0	0	0	0	0
	J2	0	0	0	0	0	0	0	0	0
	J3	0	0	0	0	0	0	0	0	0
	NO	0	0	0	0	0	0	0	0	0
	Total	0	0	0	0	0	Overall Accuracy (%)			

 β_{20}

		Actual				Accuracy indices (%)				
		J1	J2	J3	NO	Total	CE	OE	UA	PA
Predicted	J1	6	4	3	0	13	53.84615	40	46.15385	60
	J2	1	0	0	0	1	100	100	0	0
	J3	0	1	0	0	1	0	100	0	0
	NO	3	5	7	0	15	100	0	0	0
	Total	10	10	10	0	30	Overall Accuracy (%)			

 β_{30}

		Actual				Accuracy indices (%)				
		J1	J2	J3	NO	Total	CE	OE	UA	PA
Predicted	J1	7	7	5	0	19	63.15789	30	36.84211	70
	J2	2	2	1	0	5	60	80	40	20
	J3	1	1	0	0	2	100	100	0	0
	NO	0	0	4	0	4	0	0	0	0
	Total	10	10	10	0	30	Overall Accuracy (%)			

 β_{40}

		Actual				Accuracy indices (%)				
		J1	J2	J3	NO	Total	CE	OE	UA	PA
Predicted	J1	7	7	5	0	19	63.15789	30	36.84211	70
	J2	2	2	1	0	5	60	80	40	20
	J3	1	1	4	0	6	33.33333	60	66.66667	40
	NO	0	0	0	0	0	0	0	0	0
	Total	10	10	10	0	30	Overall Accuracy (%)			

 β_{50}

		Actual				Accuracy indices (%)				
		J1	J2	J3	NO	Total	CE	OE	UA	PA
Predicted	J1	8	7	5	0	20	60	20	40	80
	J2	2	2	1	0	5	60	80	40	20
	J3	0	1	4	0	5	20	60	80	40
	NO	0	0	0	0	0	0	0	0	0
	Total	10	10	10	0	30	Overall Accuracy (%)			

β_{60}

		Actual				Accuracy indices (%)				
		J1	J2	J3	NO	Total	CE	OE	UA	PA
Predicted	J1	7	6	6	0	19	63.15789	30	36.84211	70
	J2	2	3	0	0	5	40	70	60	30
	J3	1	1	4	0	6	33.33333	60	66.66667	40
	NO	0	0	0	0	0	0	0	0	0
	Total	10	10	10	0	30	Overall Accuracy (%)			46.67

Appendix 3b: Classification accuracy indices for 2.5cm_GSD_45° model on slope 1knn₅

		Actual				Accuracy indices (%)				
		J1	J2	J3	NO	Total	CE	OE	UA	PA
Predicted	J1	9	7	8	0	24	62.5	10	37.5	90
	J2	0	0	0	0	0	0	100	0	0
	J3	0	1	0	0	1	100	100	0	0
	NO	1	2	2	0	5	0	0	0	0
	Total	10	10	10	0	30	Overall Accuracy (%)			30

knn₁₀

		Actual				Accuracy indices (%)				
		J1	J2	J3	NO	Total	CE	OE	UA	PA
Predicted	J1	8	8	8	0	24	66.66667	20	33.33333	80
	J2	0	0	0	0	0	0	100	0	0
	J3	0	1	0	0	1	100	100	0	0
	NO	2	1	2	0	5	0	0	0	0
	Total	10	10	10	0	30	Overall Accuracy (%)			26.67

knn₂₀

		Actual				Accuracy indices (%)				
		J1	J2	J3	NO	Total	CE	OE	UA	PA
Predicted	J1	9	8	8	0	25	64	10	36	90
	J2	0	0	0	0	0	0	100	0	0
	J3	0	1	0	0	1	100	100	0	0
	NO	1	1	2	0	4	0	0	0	0
	Total	10	10	10	0	30	Overall Accuracy (%)			30

knn₃₀

		Actual				Accuracy indices (%)				
		J1	J2	J3	NO	Total	CE	OE	UA	PA
Predicted	J1	9	9	8	0	26	65.38462	10	34.61538	90
	J2	1	1	1	0	3	0	90	0	10
	J3	0	0	0	0	0	0	100	0	0
	NO	0	0	1	0	1	0	0	0	0
	Total	10	10	10	0	30	Overall Accuracy (%)			33.33

knn₄₀

		Actual				Accuracy indices (%)				
		J1	J2	J3	NO	Total	CE	OE	UA	PA
Predicted	J1	9	9	9	0	27	66.66667	10	33.33333	90
	J2	0	0	0	0	0	0	100	0	0
	J3	0	1	0	0	1	0	100	0	0
	NO	1	0	1	0	2	0	0	0	0
	Total	10	10	10	0	30	Overall Accuracy (%)			30

knn₅₀

		Actual				Accuracy indices (%)				
		J1	J2	J3	NO	Total	CE	OE	UA	PA
Predicted	J1	5	3	4	0	12	58.33333	50	41.66667	50
	J2	3	4	3	0	10	60	60	40	40
	J3	0	1	0	0	1	100	100	0	0
	NO	2	2	3	0	7	0	0	0	0
	Total	10	10	10	0	30	Overall Accuracy (%)			30

knn₆₀

		Actual				Accuracy indices (%)				
		J1	J2	J3	NO	Total	CE	OE	UA	PA
Predicted	J1	3	2	3	0	8	62.5	70	37.5	30
	J2	3	4	5	0	12	66.66667	60	33.33333	40
	J3	0	1	0	0	1	100	100	0	0
	NO	4	3	2	0	9	0	0	0	0
	Total	10	10	10	0	30	Overall Accuracy (%)			23.33

α_5

		Actual				Accuracy indices (%)				
		J1	J2	J3	NO	Total	CE	OE	UA	PA
Predicted	J1	2	4	4	0	10	80	80	20	20
	J2	3	2	4	0	9	77.77778	80	22.22222	20
	J3	1	2	2	0	5	60	80	40	20
	NO	4	2	0	0	6	0	0	0	0
	Total	10	10	10	0	30	Overall Accuracy (%)			20

 α_{10}

		Actual				Accuracy indices (%)				
		J1	J2	J3	NO	Total	CE	OE	UA	PA
Predicted	J1	9	9	8	0	26	65.38462	10	34.61538	90
	J2	1	1	1	0	3	66.66667	90	33.33333	10
	J3	0	0	0	0	0	0	100	0	0
	NO	0	0	1	0	1	0	0	0	0
	Total	10	10	10	0	30	Overall Accuracy (%)			33.33

 α_{15}

		Actual				Accuracy indices (%)				
		J1	J2	J3	NO	Total	CE	OE	UA	PA
Predicted	J1	9	8	8	0	25	64	10	36	90
	J2	1	1	1	0	3	66.66667	90	33.33333	10
	J3	0	1	1	0	2	0	90	0	10
	NO	0	0	0	0	0	0	0	0	0
	Total	10	10	10	0	30	Overall Accuracy (%)			36.67

 α_{20}

		Actual				Accuracy indices (%)				
		J1	J2	J3	NO	Total	CE	OE	UA	PA
Predicted	J1	9	8	8	0	25	64	10	36	90
	J2	1	2	2	0	5	60	80	40	20
	J3	0	0	0	0	0	0	100	0	0
	NO	0	0	0	0	0	0	0	0	0
	Total	10	10	10	0	30	Overall Accuracy (%)			36.67

 α_{30}

		Actual				Accuracy indices (%)				
		J1	J2	J3	NO	Total	CE	OE	UA	PA
Predicted	J1	8	8	8	0	24	66.66667	20	33.33333	80
	J2	1	2	1	0	4	50	80	50	20
	J3	0	0	1	0	1	0	90	0	10
	NO	1	0	0	0	1	0	0	0	0
	Total	10	10	10	0	30	Overall Accuracy (%)			36.67

α_{40}

		Actual				Accuracy indices (%)				
		J1	J2	J3	NO	Total	CE	OE	UA	PA
Predicted	J1	7	7	8	0	22	68.18182	30	31.81818	70
	J2	1	2	1	0	4	50	80	50	20
	J3	0	0	1	0	1	0	90	0	10
	NO	2	1	0	0	3	0	0	0	0
	Total	10	10	10	0	30	Overall Accuracy (%)			33.33

 α_{50}

		Actual				Accuracy indices (%)				
		J1	J2	J3	NO	Total	CE	OE	UA	PA
Predicted	J1	1	3	2	0	6	83.33333	90	16.66667	10
	J2	0	0	0	0	0	0	100	0	0
	J3	0	0	0	0	0	0	100	0	0
	NO	9	7	8	0	24	0	0	0	0
	Total	10	10	10	0	30	Overall Accuracy (%)			3.33

 β_{10}

		Actual				Accuracy indices (%)				
		J1	J2	J3	NO	Total	CE	OE	UA	PA
Predicted	J1	0	0	0	0	0	0	0	0	0
	J2	0	0	0	0	0	0	0	0	0
	J3	0	0	0	0	0	0	0	0	0
	NO	0	0	0	0	0	0	0	0	0
	Total	0	0	0	0	0	Overall Accuracy (%)			0

 β_{20}

		Actual				Accuracy indices (%)				
		J1	J2	J3	NO	Total	CE	OE	UA	PA
Predicted	J1	5	7	5	0	17	70.58824	50	29.41176	50
	J2	0	0	0	0	0	0	100	0	0
	J3	0	0	0	0	0	0	100	0	0
	NO	5	3	5	0	13	0	0	0	0
	Total	10	10	10	0	30	Overall Accuracy (%)			16.67

 β_{30}

		Actual				Accuracy indices (%)				
		J1	J2	J3	NO	Total	CE	OE	UA	PA
Predicted	J1	9	9	8	0	26	65.38462	10	34.61538	90
	J2	1	1	1	0	3	66.66667	90	33.33333	10
	J3	0	0	0	0	0	0	100	0	0
	NO	0	0	1	0	1	0	0	0	0
	Total	10	10	10	0	30	Overall Accuracy (%)			33.33

β_{40}

		Actual				Accuracy indices (%)				
		J1	J2	J3	NO	Total	CE	OE	UA	PA
Predicted	J1	9	7	8	0	24	62.5	10	37.5	90
	J2	1	3	2	0	6	50	70	50	30
	J3	0	0	0	0	0	0	100	0	0
	NO	0	0	0	0	0	0	0	0	0
	Total	10	10	10	0	30	Overall Accuracy (%)			40

 β_{50}

		Actual				Accuracy indices (%)				
		J1	J2	J3	NO	Total	CE	OE	UA	PA
Predicted	J1	9	7	8	0	24	62.5	10	37.5	90
	J2	1	3	2	0	6	50	70	50	30
	J3	0	0	0	0	0	0	100	0	0
	NO	0	0	0	0	0	0	0	0	0
	Total	10	10	10	0	30	Overall Accuracy (%)			40

 β_{60}

		Actual				Accuracy indices (%)				
		J1	J2	J3	NO	Total	CE	OE	UA	PA
Predicted	J1	9	7	8	0	24	62.5	10	37.5	90
	J2	1	3	2	0	6	50	70	50	30
	J3	0	0	0	0	0	0	100	0	0
	NO	0	0	0	0	0	0	0	0	0
	Total	10	10	10	0	30	Overall Accuracy (%)			40

Appendix 3c: Classification accuracy indices for slope 2 knn_5

		Actual				Accuracy indices (%)				
		B	J1	J2	NO	Total	CE	OE	UA	PA
Predicted	B	8	2	3	0	13	38.46154	20	61.53846	80
	J1	1	5	2	0	8	37.5	50	62.5	50
	J2	1	3	5	0	9	44.44444	50	55.55556	50
	NO	0	0	0	0	0	0	0	0	0
	Total	10	10	10	0	30	Overall Accuracy (%)			60

knn₁₀

		Actual				Accuracy indices (%)				
		B	J1	J2	NO	Total	CE	OE	UA	PA
Predicted	B	9	2	2	0	13	30.76923	10	69.23077	90
	J1	0	5	2	0	7	28.57143	50	71.42857	50
	J2	1	3	6	0	10	40	40	60	60
	NO	0	0	0	0	0	0	0	0	0
	Total	10	10	10	0	30	Overall Accuracy (%)			66.67

knn₂₀

		Actual				Accuracy indices (%)				
		B	J1	J2	NO	Total	CE	OE	UA	PA
Predicted	B	7	3	1	0	11	36.36364	30	63.63636	70
	J1	1	5	3	0	9	44.44444	50	55.55556	50
	J2	2	2	6	0	10	40	40	60	60
	NO	0	0	0	0	0	0	0	0	0
	Total	10	10	10	0	30	Overall Accuracy (%)			60

knn₃₀

		Actual				Accuracy indices (%)				
		B	J1	J2	NO	Total	CE	OE	UA	PA
Predicted	B	9	3	3	0	15	40	10	60	90
	J1	1	7	2	0	10	30	30	70	70
	J2	0	0	5	0	5	0	50	100	50
	NO	0	0	0	0	0	0	0	0	0
	Total	10	10	10	0	30	Overall Accuracy (%)			70

knn₄₀

		Actual				Accuracy indices (%)				
		B	J1	J2	NO	Total	CE	OE	UA	PA
Predicted	B	7	2	2	0	11	36.36364	30	63.63636	70
	J1	2	8	1	0	11	27.27273	20	72.72727	80
	J2	1	0	7	0	8	12.5	30	87.5	70
	NO	0	0	0	0	0	0	0	0	0
	Total	10	10	10	0	30	Overall Accuracy (%)			73.33

knn₅₀

		Actual				Accuracy indices (%)				
		B	J1	J2	NO	Total	CE	OE	UA	PA
Predicted	B	8	2	3	0	13	38.46154	20	61.53846	80
	J1	1	8	3	0	12	33.33333	20	66.66667	80
	J2	1	0	4	0	5	20	60	80	40
	NO	0	0	0	0	0	0	0	0	0
	Total	10	10	10	0	30	Overall Accuracy (%)			66.67

knn₆₀

		Actual					Accuracy indices (%)				
		B	J1	J2	NO	Total	CE	OE	UA	PA	
Predicted	B	8	3	1	0	12	33.33333	20	66.66667	80	
	J1	0	4	2	0	6	33.33333	60	66.66667	40	
	J2	0	3	7	0	10	30	30	70	70	
	NO	2	0	0	0	2	0	0	0	0	
	Total	10	10	10	0	30	Overall Accuracy (%)			63.33	

α_5

		Actual					Accuracy indices (%)				
		B	J1	J2	NO	Total	CE	OE	UA	PA	
Predicted	B	8	1	2	0	11	27.27273	20	72.72727	80	
	J1	1	8	5	0	14	42.85714	20	57.14286	80	
	J2	0	1	3	0	4	25	70	75	30	
	NO	1	0	0	0	1	0	0	0	0	
	Total	10	10	10	0	30	Overall Accuracy (%)			63.33	

α_{10}

		Actual					Accuracy indices (%)				
		B	J1	J2	NO	Total	CE	OE	UA	PA	
Predicted	B	9	3	3	0	15	40	10	60	90	
	J1	1	7	2	0	10	30	30	70	70	
	J2	0	0	5	0	5	0	50	100	50	
	NO	0	0	0	0	0	0	0	0	0	
	Total	10	10	10	0	30	Overall Accuracy (%)			70	

α_{15}

		Actual					Accuracy indices (%)				
		B	J1	J2	NO	Total	CE	OE	UA	PA	
Predicted	B	8	0	1	0	9	11.11111	20	88.88889	80	
	J1	2	9	1	0	12	25	10	75	90	
	J2	0	1	7	0	8	12.5	30	87.5	70	
	NO	0	0	1	0	1	0	0	0	0	
	Total	10	10	10	0	30	Overall Accuracy (%)			80	

α_{20}

		Actual					Accuracy indices (%)				
		B	J1	J2	NO	Total	CE	OE	UA	PA	
Predicted	B	8	1	2	0	11	27.27273	20	72.72727	80	
	J1	2	9	3	0	14	35.71429	10	64.28571	90	
	J2	0	0	5	0	5	0	50	100	50	
	NO	0	0	0	0	0	0	0	0	0	
	Total	10	10	10	0	30	Overall Accuracy (%)			73.33	

α_{30}

		Actual				Accuracy indices (%)				
		B	J1	J2	NO	Total	CE	OE	UA	PA
Predicted	B	8	2	4	0	14	42.85714	20	57.14286	80
	J1	2	8	2	0	12	33.33333	20	66.66667	80
	J2	0	0	4	0	4	0	60	100	40
	NO	0	0	0	0	0	0	0	0	0
	Total	10	10	10	0	30	Overall Accuracy (%)			66.67

 α_{40}

		Actual				Accuracy indices (%)				
		B	J1	J2	NO	Total	CE	OE	UA	PA
Predicted	B	7	1	4	0	12	41.66667	30	58.33333	70
	J1	2	8	2	0	12	33.33333	20	66.66667	80
	J2	0	1	4	0	5	20	60	80	40
	NO	1	0	0	0	1	0	0	0	0
	Total	10	10	10	0	30	Overall Accuracy (%)			63.33

 α_{50}

		Actual				Accuracy indices (%)				
		B	J1	J2	NO	Total	CE	OE	UA	PA
Predicted	B	2	8	5	0	15	86.66667	80	13.33333	20
	J1	0	0	0	0	0	0	100	0	0
	J2	0	0	2	0	2	0	80	100	20
	NO	8	2	3	0	13	0	0	0	0
	Total	10	10	10	0	30	Overall Accuracy (%)			13.33

 β_{10}

		Actual				Accuracy indices (%)				
		B	J1	J2	NO	Total	CE	OE	UA	PA
Predicted	B	6	4	3	0	13	53.84615	40	46.15385	60
	J1	0	2	2	0	4	0	80	0	20
	J2	0	2	0	0	2	100	100	0	0
	NO	4	2	5	0	11	0	0	0	0
	Total	10	10	10	0	30	Overall Accuracy (%)			26.67

 β_{20}

		Actual				Accuracy indices (%)				
		B	J1	J2	NO	Total	CE	OE	UA	PA
Predicted	B	7	3	4	0	14	50	30	50	70
	J1	0	6	1	0	7	0	40	0	60
	J2	0	1	4	0	5	20	60	80	40
	NO	3	0	1	0	4	0	0	0	0
	Total	10	10	10	0	30	Overall Accuracy (%)			56.67

β_{30}

		Actual				Accuracy indices (%)				
		B	J1	J2	NO	Total	CE	OE	UA	PA
Predicted	B	9	3	3	0	15	40	10	60	90
	J1	1	7	2	0	10	0	30	0	70
	J2	0	0	5	0	5	0	50	100	50
	NO	0	0	0	0	0	0	0	0	0
	Total	10	10	10	0	30	Overall Accuracy (%)			70

 β_{40}

		Actual				Accuracy indices (%)				
		B	J1	J2	NO	Total	CE	OE	UA	PA
Predicted	B	9	3	2	0	14	35.71429	10	64.28571	90
	J1	1	6	3	0	10	0	40	0	60
	J2	0	1	3	0	4	25	70	75	30
	NO	0	0	2	0	2	0	0	0	0
	Total	10	10	10	0	30	Overall Accuracy (%)			60

 β_{50}

		Actual				Accuracy indices (%)				
		B	J1	J2	NO	Total	CE	OE	UA	PA
Predicted	B	10	0	1	0	11	9.090909	0	90.90909	100
	J1	0	10	5	0	15	0	0	0	100
	J2	0	0	2	0	2	0	80	100	20
	NO	0	0	2	0	2	0	0	0	0
	Total	10	10	10	0	30	Overall Accuracy (%)			73.33

 β_{60}

		Actual				Accuracy indices (%)				
		B	J1	J2	NO	Total	CE	OE	UA	PA
Predicted	B	10	0	3	0	13	23.07692	0	76.92308	100
	J1	0	8	0	0	8	0	20	0	80
	J2	0	2	4	0	6	33.33333	60	66.66667	40
	NO	0	0	3	0	3	0	0	0	0
	Total	10	10	10	0	30	Overall Accuracy (%)			73.33

Appendix 4: Scanline measurements with an insert for discontinuity spacing measurement in a point cloud

30/11

Scanline 2 - UTM: 30M09A

DISTANCE FROM ORIGIN m	TENSURE CG (cm)	RESISTANCE (cm)	TYPE OF DISCONTINUITY A-F	DIP DIRECTION / ANGLE	TERMINATION TYPE A-C	APERTURE (cm)	JMPRING A-D	ZUBOSITUS	FAMILY SET	FOZO / OBS.
0,22 m	20cm	18,5 cm	JOINT	204 / 90 24 / 90	B	0.8cm	NONE	JRC-6-8 UNQUANTIFIED SMOOTH	F ₁	
0,47 m	11 cm	11,5 cm	JOINT	252 / 88	B	1cm	NONE	JRC-8-10 UNQUANTIFIED SMOOTH	F ₂	
0,60 m	15cm	1.5cm	JOINT	190 / 80	B	ROCK CHECKED	NONE	JRC-4-6 PLANAR SMOOTH	F _X	200/75
0,78 m	18cm	2.5 cm	JOINT	188 / 85	B	ROCK CHECKED	NONE	JRC-4-6 PLANAR SMOOTH	F _X	6/85
1,22 m	37 cm	28 cm	JOINT	40 / 75	B/A	3 cm	NONE	JRC-4-6 UNQUANTIFIED SMOOTH	F _B	
1,35 m	23,5 cm	0 cm	JOINT	260 / 90	B	2 cm	NONE	JRC-14-16 UNQUANTIFIED SMOOTH	F ₂	
1,68 m	28 cm	4 cm	JOINT	150 / 80	B	2.5 cm	NONE	JRC-4-6 PLANAR SMOOTH	F _A	
1,75 m	15 cm	4.5 cm	JOINT	34 / 82	B	3 cm				

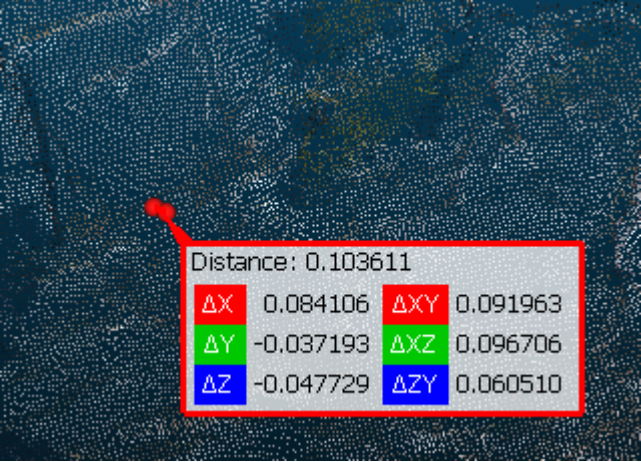
GPS coordinates Slope 276 / 95

35° 18' 37.2" N

023° 55' 14.5" E

1375 m 134
+132
214

140
+30
220



Distance: 0.103611

ΔX	0.084106	ΔXY	0.091963
ΔY	-0.037193	ΔXZ	0.096706
ΔZ	-0.047729	ΔZY	0.060510